Precambrian Research 358 (2021) 106190

Contents lists available at ScienceDirect

Precambrian Research

journal homepage: www.elsevier.com/locate/precamres

The nature of the southern West African craton lithosphere inferred from its electrical resistivity

F. Le Pape [a,*], A.G. Jones [a,b,1], M.W. Jessell [b,c], C. Hogg [a], L. Siebenaller [c,2], S. Perrouty [d], A. Touré [e], P. Ouiya [f], G. Boren [g]

[a] Dublin Institute for Advanced Studies, Ireland
[b] University of Western Australia, Centre for Exploration Targeting, Perth, Australia
[c] Université de Toulouse, CNRS, Géosciences Environnement Toulouse, Institut de Recherche pour le Développement, Observatoire Midi-Pyrénées, Toulouse, France
[d] Laurentian University, Mineral Exploration Research Centre, Harquail School of Earth Sciences, Goodman School of Mines, Sudbury, Canada
[e] BUMIGEB, Ouagadougou, Burkina Faso
[f] University of Ouagadougou, Burkina Faso
[g] University of Adelaide, Australia

ARTICLE INFO

Keywords:
West African craton
Baoulé-Mossi domain
Volta Basin
Magnetotellurics
3D inversion
Lithosphere
Geotherm

ABSTRACT

The West-African craton is defined by a combination of Archean and Palaeoproterozoic rocks that stabilised at ~2 Ga towards the end of the Paleoproterozoic Eburnean Orogeny, and therefore may reflect the transition from Archean to modern tectonic processes. Exploring its present lithospheric architecture aids further understanding of not only the craton's stability through its history but also its formation. We investigate the lithospheric structure of the craton through analysing and modelling magnetotelluric (MT) data from a 500-km-long east-west profile in northern Ghana and southern Burkina Faso crossing part of the Baoulé-Mossi Domain and reaching the Volta Basin in the south-eastern part of the craton. Although the MT stations are along a 2D profile, due to the complexity of the structures characterising the area, 3D resistivity modelling of the data is performed to obtain insights on the thermal signature and composition of the subcontinental lithosphere beneath the area. The thermal structure and water content estimates from different resistivity models highlight a strong dependence on the starting model in the 3D inversions, but still enable us to put constraints on the deep structure of the craton. The present-day thermal lithosphere-asthenosphere boundary (LAB) depth is estimated to be at least 250 km beneath the Baoulé-Mossi domain. The area likely transitions from a cold and thick lithosphere with relatively low water content into thinner, more fertile lithosphere below the Volta Basin. Although the inferred amount of water could be explained by Paleoproterozoic subduction processes involved in the formation of the Baoulé-Mossi domain, later enrichment of the lithosphere cannot be excluded

1. Introduction

The electrical resistivity structure of cratons has been studied worldwide using deep-probing electromagnetic imaging with magnetotellurics (MT), from the Slave (Jones et al., 2003), Superior (Ferguson et al., 2005) and Rae (Spratt et al., 2014) cratons in Canada, the Dharwar craton in India (Naganjaneyulu and Santosh, 2012), the Kaapvaal craton in South Africa (Evans et al., 2011; Jones et al., 2009; Miensopust et al., 2011; Muller et al., 2009), the Saõ Francisco craton in Brazil (Bologna et al., 2011; Garcia et al., 2019) to the Gawler (Curtis and Thiel, 2019; Thiel and Heinson, 2013) and Yilgarn (Dentith et al., 2018) cratons in Australia. Magnetotelluric soundings over stable Archean and Proterozoic regions significantly inform us about the structure and evolution of the subcontinental lithospheric mantle (SCLM). In the mantle, electrical resistivity will exhibit first order sensitivity to temperature (Fullea et al., 2011; Jones et al., 2013), and can therefore bring valuable insight on the lithospheric thickness of stable regions. However, most MT studies will show lateral resistivity contrasts revealing resistivity changes, not only due to temperature but also mantle water content (Yoshino et al., 2009), changes in composition (Fullea et al., 2011) as well as grain size (Jones,

* Corresponding author.
E-mail address: flepape@cp.dias.ie (F. Le Pape).
[1] Now at: Complete MT Solutions Inc., Ottawa, Canada.
[2] Now at: NGO Le Soleil dans la Main, Winseler, Luxembourg.

https://doi.org/10.1016/j.precamres.2021.106190
Received 26 September 2020; Received in revised form 11 March 2021; Accepted 15 March 2021
Available online 1 April 2021
0301-9268/© 2021 Elsevier B.V. All rights reserved.

2016; ten Grotenhuis et al., 2004) or the presence of interconnected sulphide minerals and graphite films along grain boundaries (Watson et al., 2010; Zhang and Yoshino, 2017).

In West Africa, magnetotelluric data were collected in the 1980s along profiles in Niger (Ritz, 1983), Senegal (Ritz and Robineau, 1988) and Mauritania (Ritz et al., 1989), highlighting mantle resistivity contrasts between the West African Craton (WAC) and its margins. In Senegal, deep MT soundings (up to 10,000 s) interpreted the presence of a thick resistive lithosphere extending down to 250 km beneath the WAC and transitioning into 175 km thick lithosphere under the Mauritanides orogenic belt (Ritz and Robineau, 1988). Due to the sparsity of broadband seismic stations in West Africa and also the lack of local seismic events, the main seismic information about the lithosphere has been derived from continental-scale to global seismic tomography studies (e.g., Fishwick, 2010; Pasyanos and Nyblade, 2007; Priestley et al., 2008; Schaeffer and Lebedev, 2013). Although they might lack resolution, they offer a broad understanding of the structure of the craton lithospheric structure (Jessell et al., 2016), imaging fast and thick lithosphere beneath the WAC to about 250 km on average, in agreement with the 1980's resistivity models. More recently, Celli et al. (2020) confirmed the two separate lithospheric units previously highlighted by Jessell et al. (2016) beneath the Leo-Man and Reguibat Shields, with a high velocity lithospheric root reaching at least 260 km in the southern part of the WAC. Extraction of seismic group velocity from combined earthquake and seismic ambient noise data has been investigated to improve seismic tomography resolution on the WAC, but is still a work in progress (Ouattara et al., 2019).

Heat flow measurements on the WAC (Lesquer and Vasseur, 1992) suggest differences in lithosphere thickness between the WAC and surrounding mobile belts, with low heat flow density values of 33 +/- 8 mWm^{-2} for the southern part of the craton and values of 51 +/- 8 mWm^{-2} for the surrounding Pan-African belt. The Leo-Man Shield (Fig. 1) is intruded by clusters of Neoproterozoic age and more abundant Jurassic age kimberlites revealing a more depleted SCLM in Neoproterozoic time compared to the Jurassic (Skinner et al., 2004). The Koidu kimberlite complex in Sierra Leone comprises the most studied xenoliths, indicating a paleo-geotherm corresponding to a 38–40 mWm^{-2} surface heat flow for the Archean Man Shield (Fung and Haggerty, 1995; Smit et al., 2016). Those values suggest the presence of a thick lithospheric root (>200 km) at the time of the Koidu kimberlite eruption (146 Ma). In the area, eclogitic alluvial diamond formations were dated to the Neoproterozoic (~650 Ma) at the time of the assembly of Gondwana (Smit et al., 2016). In Ghana, although not dated, deep peridotitic diamonds from the alluvial deposits of Akwatia have been associated to a paleo-geotherm corresponding to a 40–42 mWm^{-2} surface heat flow indicating also the presence of a thick lithospheric root below the Proterozoic Baoulé-Mossi Domain at the time of their formation (Stachel and Harris, 1997).

In this study we discuss deep present-day constraints provided by magnetotellurics (MT) on the lithospheric structure of the

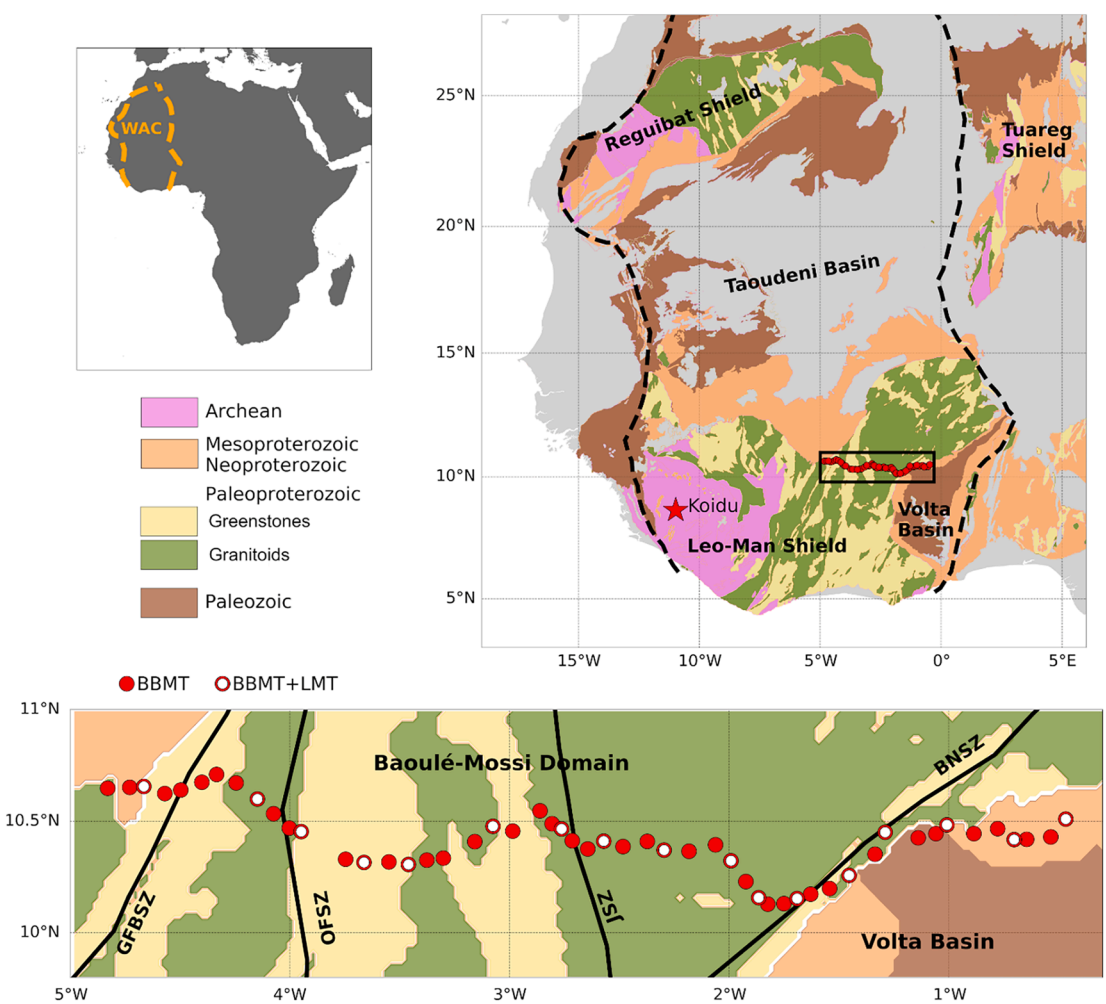

Fig. 1. Study area and location of the MT profile (52 sites) with respect to the regional lithologies and tectonic features (map based on WAXI geological database). GFBSZ = Greenville-Ferkessedougou-Bobo-Dioulasso shear zone, OFSZ = Ouango-Fitini shear zone, JSZ = Jirapa shear zone, BNSZ = Bole-Nangodi shear zone. BBMT = broadband MT; LMT = long period MT. MT stations IDs can be found on Fig. 3.

Neoproterozoic Baoulé-Mossi Domain located in the southern part of the West African craton. The MT survey was carried out in 2013 as part of Phase 2 of the West African Exploration Initiative (WAXI) project, and comprises a single 500-km-long east–west profile crossing a variety of complex shear zones and sutures from southern Burkina Faso to northern Ghana (Fig. 1). This profile defines an extension of previously published resistivity modelling in Burkina Faso (Le Pape et al., 2017) including deeper soundings (>1000 s) and data from Ghana. After performing data processing, 3D resistivity modelling and resolution tests, we discuss the lateral changes in the model resistivity structure of the SCLM beneath the area and how our results bring further insight into the evolution of the Leo-Man lithosphere.

2. Tectonic and geological setting

The West-African craton is defined by a combination of Archean and Paleoproterozoic rocks that stabilised at ~2 Ga towards the end of the Eburnean Orogeny. Mainly covered by Neoproterozoic and younger sedimentary sequences, the Archean and Birimian basements are only exposed throughout the Reguibat shield in the north and Leo-Man shield in the south (Barth et al., 2002; Boher et al., 1992; Ennih and Liégeois, 2008). The upper crustal limits of the craton are defined by the surrounding Pan-African and Hercynian orogenic belts (Barth et al., 2002; Lesquer et al., 1984; Villeneuve, 2008). Following the Eburnean orogeny (2.21 – 2.07 Ga), the area was thought to have experienced very little activity between 1.7 Ga and 1.0 Ga enabling the cratonisation and development of a thick lithosphere (Ennih and Liégeois, 2008). However, this interpretation has been challenged recently as widespread mafic intrusive events have been catalogued for the WAC ranging from 1.8 Ga to 200 Ma (Baratoux et al., 2019; Jessell et al., 2015), although they do not represent significant strain. During the Neoproterozoic, extensional events associated with continental breakup affected the WAC. They were followed by the main Pan-African orogenic phase (~600 Ma) that led to convergence on all the WAC boundaries, including the Anti-Atlas in the north and the Trans-Saharan belt to the east, and relocated other cratonic regions to the east of the WAC in the Tuareg Shield (Ennih and Liégeois, 2008). In the Mesozoic (~200 Ma), southern and western parts of the craton were affected by the Atlantic rift and associated extensive volcanism (Baratoux et al., 2019; Marzoli et al., 1999).

The Leo-Man and Reguibat Shields (Fig. 1) are separated by the vast (>1 M km^2) Taoudéni Basin that covers most of the western Sahara with Mesoproterozoic to Paleozoic aged sedimentary rocks (Bronner et al., 1980; Deynoux et al., 2006; Rooney et al., 2010). In the south-eastern part of the WAC, the Volta Basin (Fig. 1) mainly consists of late Neoproterozoic sedimentary rocks unconformably overlying the Palaeoproterozoic basement of the Leo-Man block (Kalsbeek et al., 2008). The different sedimentary groups have been interpreted to originate from either a passive margin deposition setting or foreland basin deposition in association with the opening and closure of the Pan-African Ocean (Deynoux et al., 2006; Kalsbeek et al., 2008). The Leo-Man Shield defines the southern part of the West African craton (WAC). It is characterized by an Archean nucleus (3.6–2.7 Ga) mainly exposed in Guinea, Sierra Leone and Liberia, and bounded by the Paleoproterozoic (2.2–2 Ga) Baoulé-Mossi Domain exposed over most of the Ivory Coast and Burkina Faso (Baratoux et al., 2011; Barth et al., 2002; Boher et al., 1992). The Baoulé-Mossi Domain (Fig. 1), which is the main focus of this study, exhibits Archean-like greenstone-granitoid assemblages consisting of Birimian volcano-sedimentary belts separated either by extensive intermediate-felsic intrusive igneous provinces associated with the Eburnean orogeny or by flysch-like basins whose basement is unknown (Baratoux et al., 2011; Block et al., 2016; Feybesse et al., 2006). The N-S oriented greenstone belts and granitoid domains of the Baoulé-Mossi Domain are associated with large scale N-S shear zones (Fig. 1), such as the Greenville-Ferkessedougou-Bobo-Dioulasso shear zone (GFBSZ) and the Ouango-Fitini shear zone (OFSZ), and likely extend throughout the crust and the lithospheric mantle of Burkina Faso (Baratoux et al., 2011; Le Pape et al., 2017). To the east, in north-west Ghana, the N-S Jirapa shear zone (JSZ) located east of the Wa-Lawra belt merges with the southern extension of the NE-SW Bole-Nangodi shear zone (BNSZ) (Block et al., 2015).

3. Magnetotellurics

3.1. Data acquisition and processing

The MT time series data were collected between February and May 2013 using both broadband (BBMT) and long period (LMT) magnetotelluric instruments. The LMT stations are separated by around 30 km on average, and the BBMT instruments define an approximate 10 km spacing along the profile. The WAXI MT profile (Fig. 1) is characterized here by a total of 52 BBMT sites and 17 LMT stations. The BBMT data were recorded over three days with broadband Phoenix Geophysics (Toronto) MTU-5A systems with MTC-50H coils, and processed with the standard robust processing of the commercial code from Phoenix Geophysics based on Wight and Bostick (1980) cascade decimation plus Jones and Jödicke (1984) robust algorithm, which is a Least Trimmed Squares robust technique proposed independently by Rousseeuw (1984). The LMT data were recorded for an average of 20 days using LEMI-417 M (Lviv Centre of Institute for Space Research) instruments with ring-core fluxgate magnetometers, and processed following the processing method of Smirnov (2003). The LMT data were processed for time series recorded only during the night-time due to the local source effects of the equatorial electrojet (see next section). We used remote referencing methods (Gamble et al., 1979) to reduce bias effects and improve the quality of the estimated MT responses. At common locations, BBMT and LMT were merged for periods between 100 and 1,000 s, considering the broadband data as the shifting reference, i.e., the LMT apparent resistivity curves were shifted to match the BBMT curves, although overall the data overlap very well. For this study, mainly focused on the lithosphere structure, we limit the periods of investigation from 0.1 s to 10,000 s.

3.2. Equatorial electrojet

Natural MT sources are defined by complex ionospheric and magnetospheric current systems (Viljanen, 2012). At many locations on the Earth and for most of the time the MT plane wave assumption is valid, but the presence of localized current sources in the ionosphere, intensified during enhanced magnetospheric activity, brings a non-homogeneous characteristic in the MT source (Mareschal, 1986) that can lead to erroneous data interpretation (e.g., Jones and Spratt, 2002). The daytime equatorial electrojet (EEJ) occurs every day as a consequence of the Solar Quiet day current systems, called Sq, that rotate differentially in the northern and southern hemispheres leading to current flow centred on the magnetic dip equator varying in width and intensity with geographical location. During the northern hemisphere Summer, the flow of the EEJ current is eastwards, and during the Winter is westwards (Yamazaki and Maute, 2017). Its effects on MT responses at longer periods collected in low latitude regions cannot be ignored (Carrasquilla and Rijo, 1998). For instance, Padilha et al. (1997) showed that EEJ source effects appear at shorter periods in resistive regions than for conductive regions. For the WAXI MT data, EEJ effects are mainly observed for periods above 1,000 s (Fig. 2), therefore during processing, the BBMT data were considered unaffected and only the LMT sites were processed taking the EEJ into account.

The EEJ being only a daytime event, the WAXI long period MT data were reprocessed considering both nights-only (1800–0600 + 1 day local time) and days-only (0600–1800 local time) time series in order to compare the effects of the EEJ on both apparent resistivities and phases (Fig. 2). Time series of the recorded magnetic induction show an enhanced magnetic amplitude during the day that is very strong on the

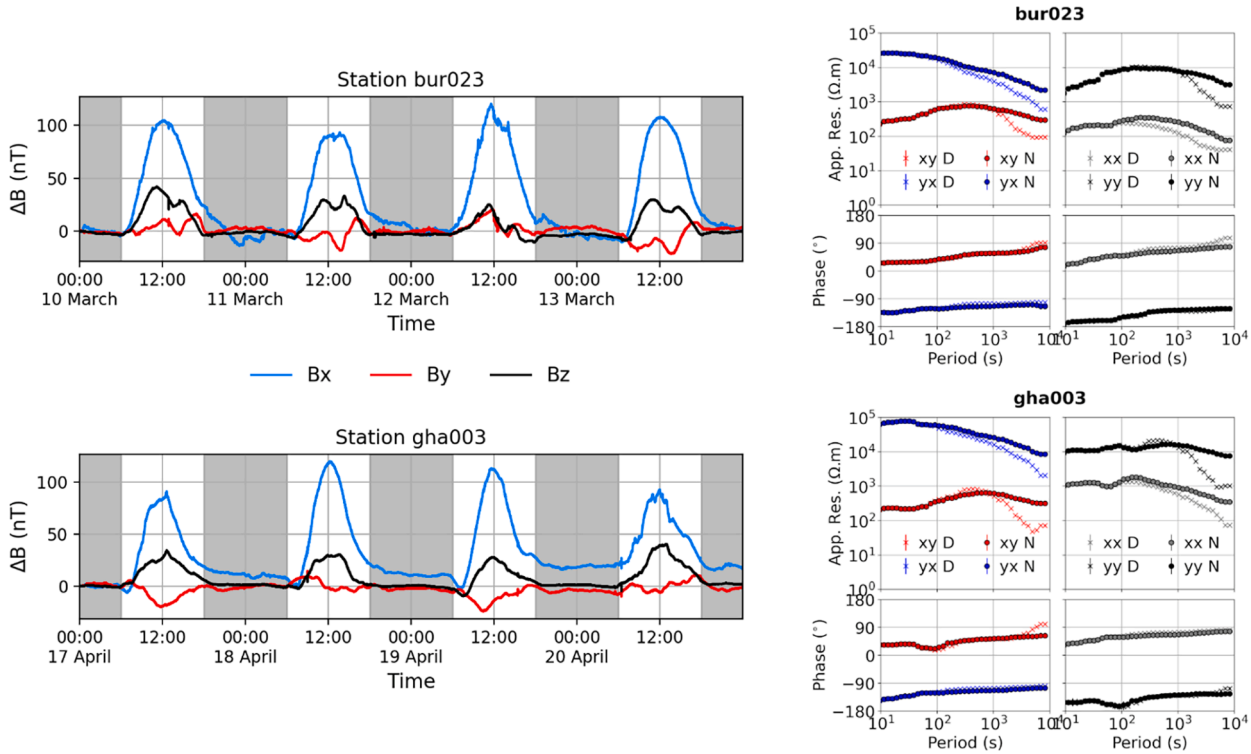

Fig. 2. Effects of the equatorial electrojet (EEJ) on the MT data. Those effects are illustrated on short windows of recorded magnetic induction time series (left panel), and apparent resistivity and phase (right panel) for selected MT sites. All four impedance components are shown for both nights-only (N) and days-only (D) processed data for periods from 10 s to 10,000 s.

N-S component (Bx) in response to the E-W orientation of the electric currents (Ey) associated with the EEJ. As a result, on the processed MT responses there is a consistent drop in the apparent resistivity for periods over 1,000 s seen on the daytime (D) responses for stations located throughout the whole profile. This effect is illustrated on Fig. 2 for two sites located in different parts of the profile, showing how all components are affected by the equatorial electrojet. As a result, we only considered LMT data processed for time series recorded during the night-time (N) in the data analysis and 3D modelling. It is worth mentioning that although by considering night-time data we strongly mitigate the EEJ effect on the data, some minor contributions might still be present. Although Sq currents are expected to vanish during the night, the night times considered do not fully exclude all Sq contributions. An alternative would be to properly model the EEJ source in order to remove its effect directly from the data, but that would introduce further uncertainties and also requires an existing global resistivity model for the area. It was therefore considered beyond the scope of this study.

3.3. Dimensionality and distortion of the MT data

Most sites appear fairly 3D, exhibiting high values of apparent resistivity for all four components of the impedance tensor but also showing repetitive out-of-quadrant phases for a number of sites (Fig. 3a). The data reveal recurrent distortion signatures in the signal highlighted by the V-shaped apparent resistivity curves associated with extreme phases. Those effects can be seen for several neighbouring sites and are more than likely not related to noise issues but to very strong distortion at the regional scale. Although the observed anomalous phases could be explained by the presence of anisotropy (Heise and Pous, 2003), due to their repetitive behaviour across multiple sites affecting all components, we assumed more likely an origin caused by regional 3D features. In fact, relatively simple and realistic 3D models have shown that, in the presence of high resistivity contrasts, reversed current channelling in comparison to the regional flow direction can lead to anomalous phases on the data: L-shaped conductor model (Ichihara and Mogi, 2009) and 3D "folded" conductor (Autio and Smirnov, 2020; Egbert, 1990). Real case studies over Archean-Proterozoic terrains have also highlighted the presence of out-of-quadrant phases and have shown that 3D inversion can deal with those effects (Bologna et al., 2017; Piña-Varas and Dentith, 2018; Thiel et al., 2020).

Despite an overall consistency in the statics between neighbour sites, a few sites likely exhibit static shifts in the apparent resistivity curves (e.g., large differences between the levels of the apparent resistivity xy and yx curves). We can see that major splits on apparent resistivity curves occur for stations at the vicinity of major tectonic shear zones: stations around BUR022 (Supplementary Fig. S1) located near the OFSZ and stations around gha003 (Supplementary Fig. S2) located near the JSZ. Here, we decided to let the 3D inversion handle the static shift problem, including conductive and resistive features near the surface of the model grid (Patro and Egbert, 2011). It is not optimal, particularly with a coarse grid but without *a priori* information and in this case highly complex data, the static shift problem can be very tricky to determine. For instance, at a single site not all curves may necessarily be affected and sometimes just one or two components could be shifted up or down.

In order to investigate further the dimensionality of the data we apply phase tensor analysis (Caldwell et al., 2004). We recognise that phase tensors are unstable in the presence of noise or high distortion (Jones, 2012), and due to the non-representation of error only used them in a qualitative sense. The components of the phase tensor are usually represented as an ellipse that has its axes parallel and perpendicular to the strike direction in isotropic 2D cases. In 3D cases, the coordinate-invariant skew angle defines the deviation of the phase tensor principal axes from an equivalent symmetric configuration resulting from the asymmetry of the phase responses produced by 3D structures (Heise et al., 2006). For the WAXI MT data, the skew angles show values outside the [−5°- 5°] interval for a significant number of periods at most

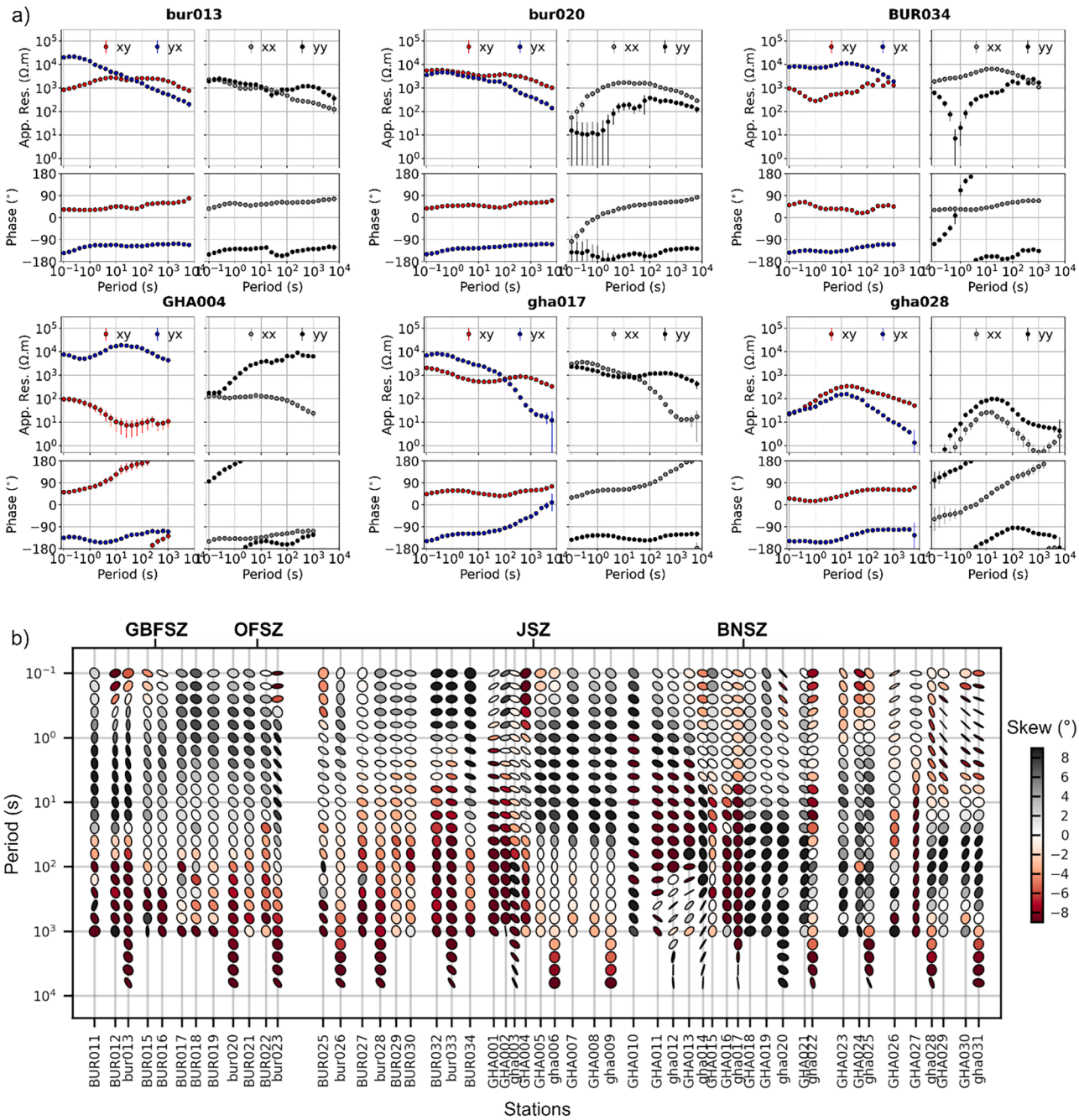

Fig. 3. a) MT data for 6 selected stations along the profile. The full data plots can be found in Supplementary Figures S1-S5. b) Phase tensor analysis for the full MT profile highlighting the dimensionality of the data. Stations are listed from west to east and their locations can be found on Fig. 1. The phase tensor skew analysis was performed using the MTpy package (Kirkby et al., 2019; Krieger and Peacock, 2014).

sites, exceeding the limits of 2D approximations for reasonable quality MT data (Fig. 3b). In addition, in a 2D setting the orientation of the ellipses would also be expected to remain consistent between site and periods, this is not the case here. The complex 3D signatures of the phase tensor ellipses previously observed for southern Burkina Faso (Le Pape et al., 2017) extend to northern Ghana as well as at longer periods. Although, the data show some 2D-like behaviour for clustered sites and periods, as discussed above the consistent site-to-site and period-to-period 3D signature is too broad and significant to be neglected.

3.4. 3D resistivity modelling

Having only a "single-profile" station layout we are aware this is not an optimal approach for 3D inversion, although advantages in 3D inversion of profile data have been shown (Siripunvaraporn, 2012). Here, due to the significant 3D signatures of the responses for a broad range of MT stations, we decided to use the parallel nonlinear conjugate gradient (NLCG) 3D inversion code ModEM3DMT (Egbert and Kelbert, 2012; Kelbert et al., 2014). Inversion input files, mesh and starting model were generated using the *MTpy* package (Kirkby et al., 2019; Krieger and Peacock, 2014). The 3D mesh used in the inversions (Fig. 4a) is defined by 49 × 154 × 75 cells, with a horizontal grid space of 4 × 4 km around the stations. The starting *a priori* model used for the inversion (Fig. 4a) comprises a 500 Ωm layer down to 150 km with a gradual decrease of resistivity with depth reaching 100 Ωm at 300 km and 10 Ωm at 410 km. This model was built on the *a priori* information

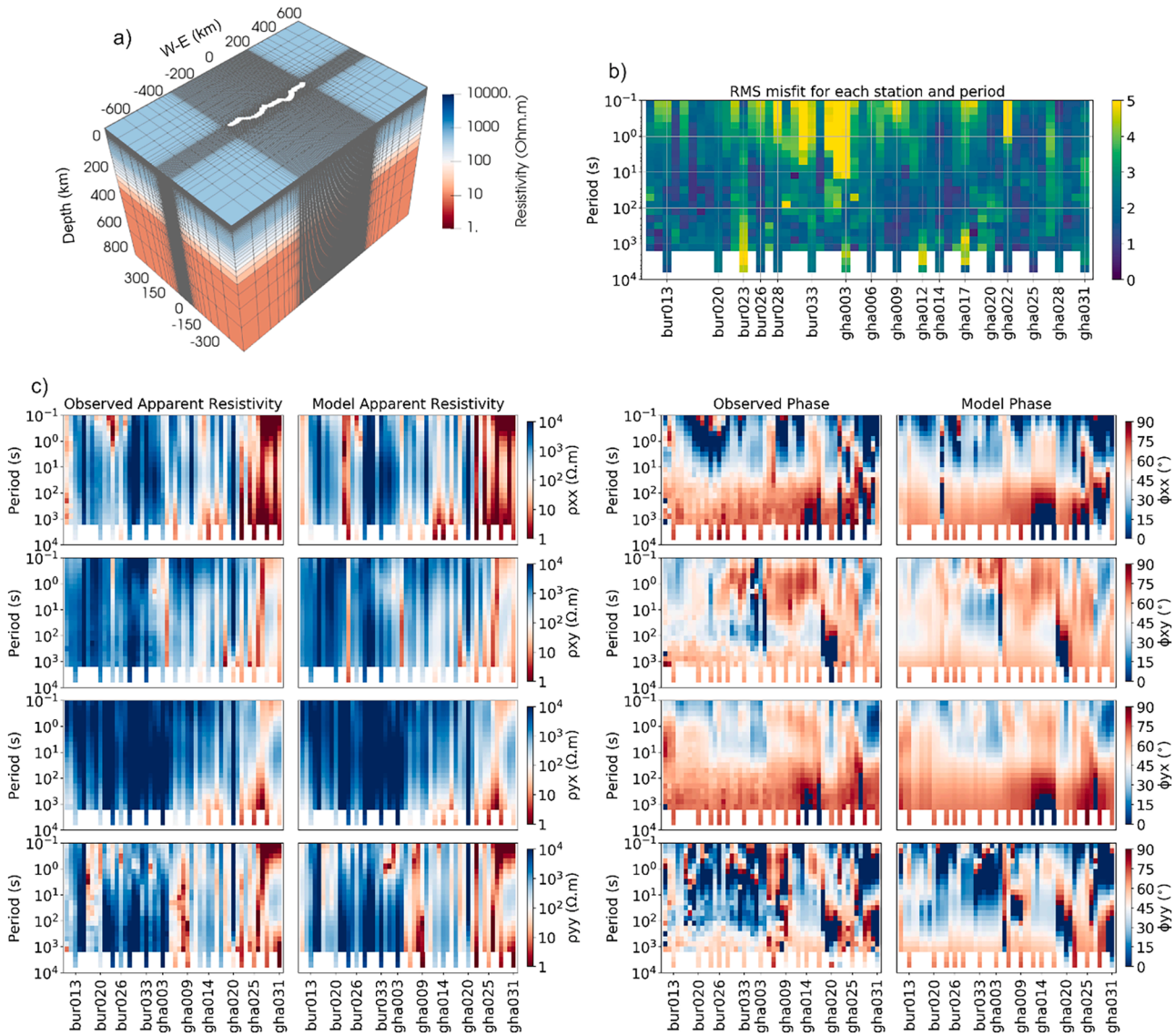

Fig. 4. a) Starting *a priori* model used for the 3D inversion; b) RMS misfit per period/stations for the final model. c) Pseudosections for each component of observed vs modelled apparent resistivity and phase.

that the lithosphere beneath the study area is quite thick but also with the goal to avoid too sharp contrasts between "*a priori*" layers. While higher covariance values in the inversion will result in a smoother model, lower covariance values will lead to rougher models including more small-scale features (Robertson et al., 2020). Here, a covariance value of 0.4 was used for both horizontal and vertical directions as it showed a nice trade-off towards a relatively smooth model that fits the data with an acceptable global Root Mean Square (RMS) misfit of 2.77.

The data were inverted simultaneously for all four impedance tensor components using an error floor value of 0.05 * sqrt(|ZxyZyx|) for each impedance tensor element. This is equivalent to a phase error floor of 2.8° and an apparent resistivity error floor of 10%. Since the vertical component of the magnetic field was only recorded for the long period stations and due to the strong effects from the EEJ on the long period magnetic data, tipper data was not included in the inversion. Periods ranging from 0.1 s to 10,000 s were modelled for both crustal and lithospheric structures beneath the profile. The 3D inversion was performed in multiple steps in order to progressively modify the starting model:

(i) long period inversion only (10–10,000 s);
(ii) all periods (0.1–10,000 s) inversion using the best model (low RMS but no overfitting) obtained in step (i) as the starting model;
(iii) all periods (0.1–10,000 s) inversion using an intermediate model (RMS = 3) from step (ii) as the starting model.

As mention above the data are quite complex and for some sites the model cannot fit perfectly all components (Fig. 4b-c and Supplementary Fig. S1-S5), particularly at shorter periods for a few stations in the middle of the profile. However, the overall fit to apparent resistivity and phase at each period and for each component remains acceptable. In addition, it is reassuring to see that some of the most distorted sites exhibiting extreme phases (e.g. BUR034) can be properly handled by the 3D inversion (Supplementary Fig. S2). Depth slices from 10 km to 100 km, as well as a vertical cross-section through the final 3D resistivity model, are shown on Fig. 5. The different observed features for the crust and upper lithospheric mantle but also sensitivity to deeper structures (>100 km) and resolution of the deep lithosphere are discussed in the following section.

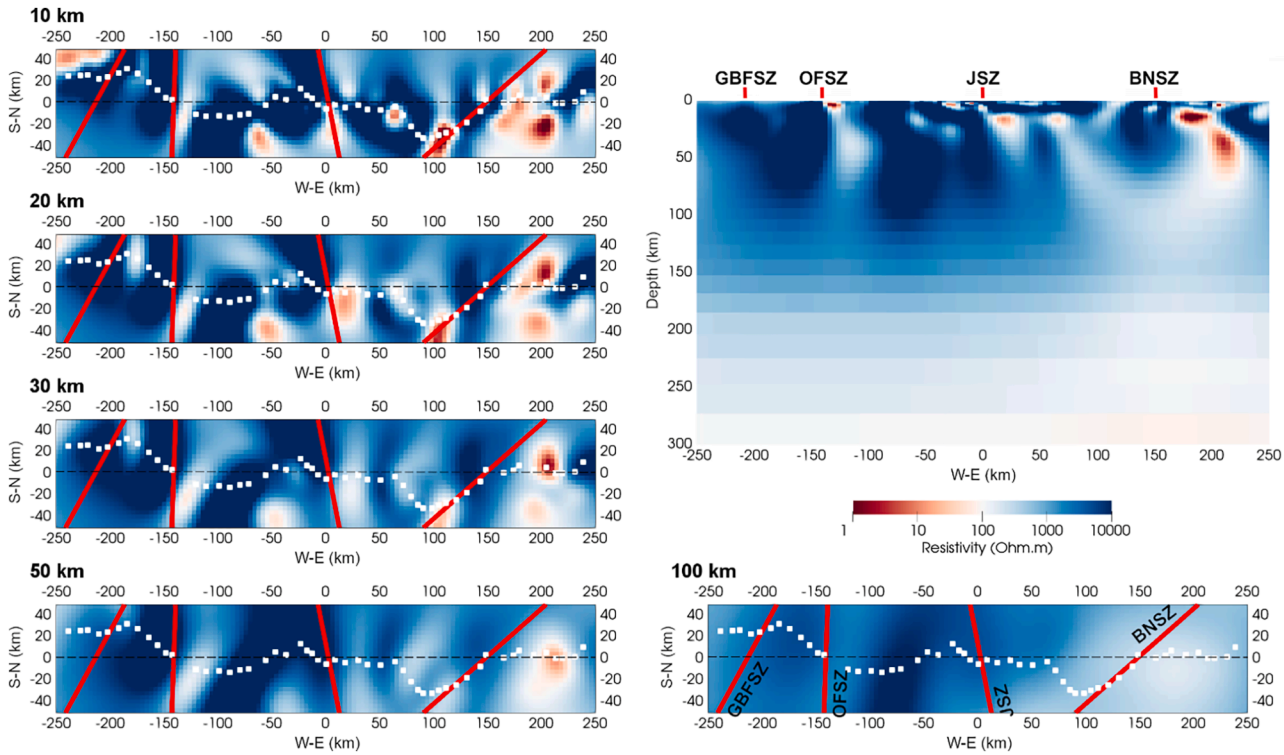

Fig. 5. 3D resistivity structure beneath the WAXI MT profile shown as horizontal slices down to 100 km and vertical cross-section located along the dashed black line. Red lines represent the shear zones surficial traces described in Fig. 1.

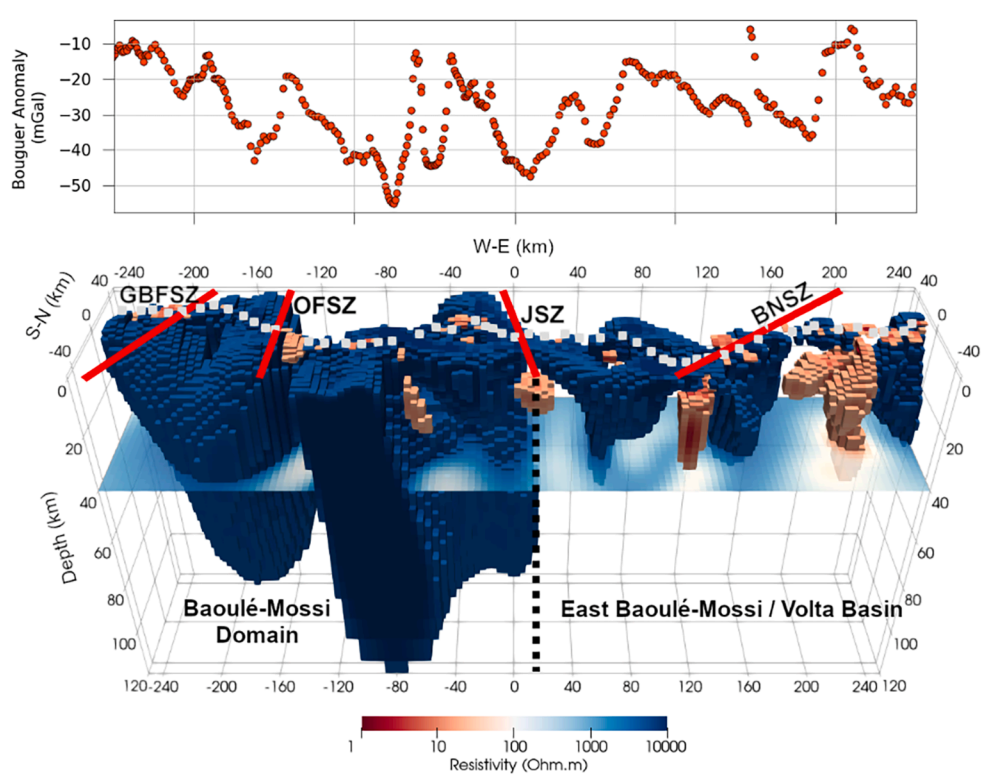

Fig. 6. Bouguer anomaly along the profile and 3D visualisation of the resistivity model showing dominant resistive (>5000 Ωm) and conductive (<30 Ωm) structures for the crust and upper mantle. Gravity profile collected along the same road as MT and projected here on x = 0.

4. Interpretation of the 3D resistivity model

4.1. Crust and upper mantle structure

The resistivity structure of the crust of southern Burkina Faso is discussed in detail in Le Pape et al. (2017). Here our main focus is on crustal features that extend into the upper mantle and also on the lithospheric differences between southern Burkina Faso and northern Ghana. There is clear difference in the overall resistivity of the crust and upper mantle between the western (~10,000 Ωm at 50 km) and eastern (~1,000 Ωm at 50 km) halves of the profile, which becomes significant at depths more than 30 km (Fig. 5). The resistivity contrast is apparent already in the data, namely on the apparent resistivity pseudo-sections (Fig. 4c).

The Wa-Lawra belt and associated Jirapa shear zone (JSZ) correlates with the resistivity transition in the lower crust and upper mantle. In addition to the JSZ, the main shear zones in the area, defined by the Greenville-Ferkessedougou-Bobo-Dioulasso shear zone (GFBSZ) and the Ouango-Fitini shear zone (OFSZ), are likely extending in the upper mantle, as their surficial traces coincide with more conductive material separating highly resistive blocks (Fig. 5). It is worth noting that the main conductive anomalies are located in the crust and in the vicinity of the main shear zones, defined as steeply east dipping (Baratoux et al., 2011). Furthermore, in the upper mantle (~100 km) on the eastern side of the profile, the NE-SW resistivity contrast matches the orientation of the Bole-Nangodi shear zone (BNSZ). The orientation is reasonably well-defined given that the station locations in this part of the profile follow the trace of the BNSZ. This is an interesting observation since the shallower structures in the crust of northern Ghana seem to follow a N-S orientation similarly to southern Burkina Faso (Fig. 5).

On Fig. 6, in order to highlight differences in resistivity between the west and east of the profile, only resistive blocks above 5,000 Ωm and conductive blocks below 30 Ωm are shown. Based on the lateral changes in the resistivity beneath the profile, two zones are defined: the Baoulé-Mossi Domain and East Baoulé-Mossi/Volta Basin (Fig. 6). They will be discussed in detail in the following section. The 3D view of Fig. 6 clearly shows the connection of the GFBSZ, the OFSZ and the JSZ with the upper mantle. Estimation of the electrical Moho depth remains inconclusive due to the high resistivity of the crust and lithospheric mantle, particularly on the western side of the profile, but the highly resistive blocks of northern Ghana, east of the JSZ, seem to be mainly located in the crust.

The lithospheric mantle resistive block delimited by the surficial signature of large scale shear zones (Fig. 6) could be interpreted as the remnant nappe stacking formations of the Baoulé-Mossi during the Eburnean orogeny (Baratoux et al., 2011; Block et al., 2015). The most significant conductive anomaly is observed in the crust of Ghana, on the eastern end of the profile (Figs. 5 and 6). In a geologically old area such as West Africa, the known candidates for conductive anomalies are mostly related to the presence of graphite located in shear zones or carbon films interconnected along grain boundaries, stable and conductive above the graphite-diamond stability depth of around 150 km in a present-day cratonic geotherm (Selway, 2014). Sulphide minerals deposited from past metasomatism and magmatic events are also potential candidates. The Bouguer gravity anomaly along the profile was discussed in Le Pape et al. (2017); the trends in the gravity anomaly follow the trends in greenstone belts and granitoid domains of southern Burkina Faso, an observation likely also valid for northern Ghana with the Baoulé-Mossi Domain extending under the Volta Basin. However, it is worth noting that the largest positive peak anomaly in Bouguer gravity along the whole profile seems to coincide with the dominant conductive anomaly in the crust beneath the Volta Basin. Although no clear conclusions can be drawn, the presence of such dense conductive material in the crust could favour an interpretation towards the presence of magmatic sulphide deposits.

4.2. Resolution of the deep lithosphere

In this section we investigate the limits in the model resolution at depth and also the impact of using different *a priori* information in the 3D inversion for the deeper resistivity structure of the model. Do to so, we consider four alternate inversion models, each of them obtained from a different starting model. For each starting *a priori* model, the resistivity of the upper 100 km is fixed and directly taken from our reference 3D model discussed above (Fig. 5), but differs for the deep lithosphere (>100 km). By modifying the initial inversion model below 100 km, we can determine how the deep lithosphere structure can be recovered from inversion and how the results actually strongly depend on the starting/*a priori* resistivities (Fig. 7). For example, whereas the results clearly show in all four cases that resistive material is required at depth by the inversion, the changing deep structures of each model clearly highlight the non-uniqueness of the inversion process. It is also worth noting that the RMS misfit at each station for each inversion is very close to the original model misfit, if not slightly improving it. This provides some comfort that the models sensitivity at depth is relatively robust and confirms the presence of a thick resistive lithosphere beneath the Baoulé-Mossi domain. In addition, the presence of the conductive anomaly in the crust of northern Ghana is likely limiting the resolution to further depths in this section of the profile. However, despite different starting models, the inversions consistently recover a thinner more conductive lithosphere in the easternmost part of the profile associated with improved RMS misfit. It might be difficult to constrain the deep lithosphere resistivity in this part of the profile, but there is a clear difference in the mantle structure compared to the western part that is recurrent on all four inversions.

At the base of the lithosphere and transition into the asthenosphere, the resistivity of dry peridotite is expected to modulate around 100 Ω.m, a value that can be used as a resistivity proxy for the mantle adiabat (Evans et al., 2011). Lower resistivity (higher conductivity) values suggest the presence of melt or high hydrogen content (Selway et al., 2019), which, as seen on Fig. 7, is beyond the constraints of our 3D inversions. Since we are only targeting a lower bound on the thermal signature and water content of the lithosphere, in the following section we discard the most conductive model A, but compare further the mantle resistivity structure of the reference model, model B, model C and model D in order to characterize further the SCLM structure beneath the profile.

4.3. SCLM thermal signature and water content

Having only modelled one profile in 3D, we understand and appreciate the lateral resolution issues and therefore interpretation limitations of our approach. However, we believe that conclusions can still be drawn and discussed from the WAXI MT experiment in terms of the SCLM composition (enriched vs. depleted) and also on the water content of the lithospheric mantle. We do not aim here to perform a full petrological modelling of the area, but to at least discriminate between dry depleted lithosphere or more enriched lithosphere with a lower bound on water content. To do so, we need an approximate geotherm for the area as well as a mantle composition model for interpreting the observed mantle conductivity values. The mantle resistivity derived from MT can provide a reasonable approximation of the present-day geotherm in the area of interest (Muller et al., 2009). Based on heat flow density values of 33 +/- 8 mWm^{-2} for the Leo-Man shield (Lesquer and Vasseur, 1992), and a Jurassic heat flow value of 38 mWm^{-2} for the Koidu Kimberlite derived from clinopyroxene xenocrysts (Smit et al., 2016), we consider here the geotherm models from Hasterok and Chapman (2011) associated with a heat flow value of 40 mWm^{-2}, defined as a reference for Precambrian regions by the same authors, and a heat flow value of 35 mWm^{-2} (Fig. 8a).

For modelling the bulk mantle resistivity (inverse of conductivity), we use the Hashin-Shtrikman (HS) bounds for multi-phase materials

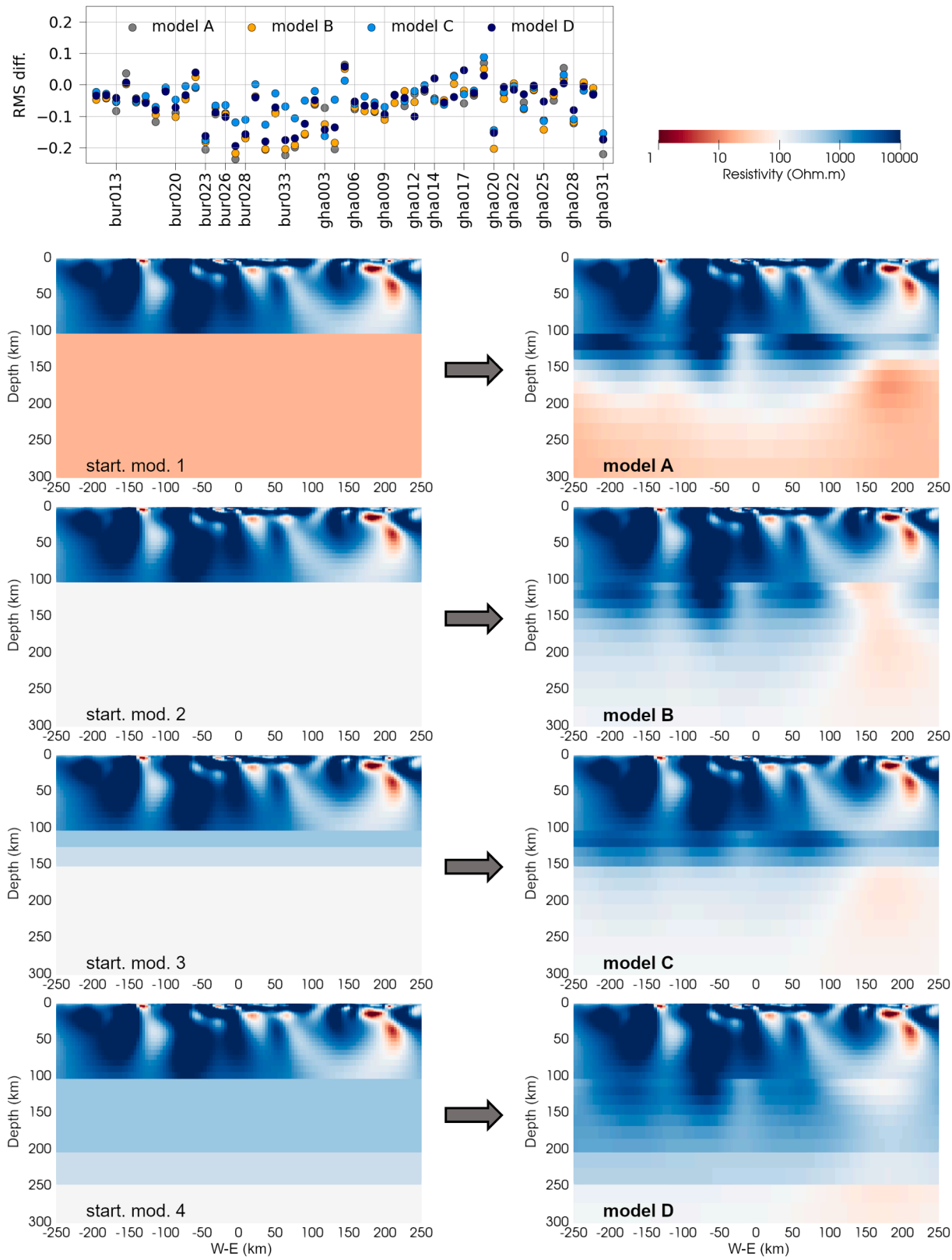

Fig. 7. Alternative models obtained after inversion using different starting/*a priori* models for the deep lithosphere. Each starting model shares locked resistivity values from the reference model for the top 100 km layer and a resistivity of 10 Ωm below 410 km. The RMS difference (RMS diff.) represents the inversions RMS deviation from the reference model (Fig. 5) misfit at each station for the four alternative models.

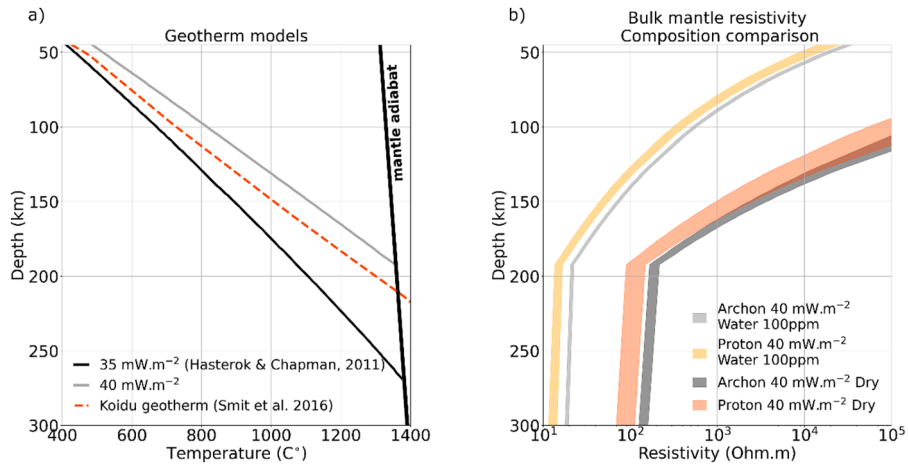

Fig. 8. a) Geotherm models based on Archean/Proterozoic heat flows and xenolith data from the WAC; b) Effects of mantle mineral composition and bulk water content on bulk mantle resistivity calculated using Eqs. (1) and (2). Each zone is defined by upper σ^{+}_{HS} and lower σ^{-}_{HS} bounds associated with different mantle composition and water content.

(Berryman, 1995) that have been previously used for modelling lithospheric mantle conductivities (Fullea et al., 2011; Jones et al., 2012). The lower bound σ^{-}_{HS}, which assumes a resistive matrix with no interconnected conductive inclusions, is defined as:

$$\sigma^{-}_{HS} = \left(\sum_{k=1}^{N} \frac{x_k}{\sigma_k + 2\sigma_{min}}\right)^{-1} - 2\sigma_{min}, \tag{1}$$

with N representing the number of mineral phases, σ_k each phase conductivity, x_k the mineral phase proportion and σ_{min} the minimum phase conductivity. The higher bound σ^{+}_{HS} is defined by the same equation replacing σ_{min} by the maximum conductivity σ_{max}. Furthermore, we use the general equation from Fullea et al. (2011) to estimate the conductivity σ_k of each mantle mineral phase defined as:

$$\sigma_k = \sigma_0 exp\left(\frac{-\Delta H(X_{Fe}, P)}{k_b T}\right) + \sigma_{0i} exp\left(\frac{-\Delta H_i}{k_b T}\right) + \sigma_p \tag{2}$$

In Eq. (2), the first term represents the small polaron conduction (i.e., electrons hopping between Fe^{3+} and Fe^{2+} ions) with dependency on the iron number X_{Fe}, the second term defines the contribution of ionic conduction by Mg vacancies at high temperatures and the last term σ_p describes proton conduction associated with the presence of water. Here, for the proton conductivity σ_p, we use the olivine conductivity model from Jones et al. (2012) which was calibrated by field geophysical observations, the model of Dai et al. (2009a) for both orthopyroxene and clinopyroxene, and the garnet model from Dai et al. (2009b). Various xenoliths and laboratory studies usually exhibit a wide range of values for water partition coefficients between each mineral phase (Fullea, 2017). Here we decided to consider a global average for each coefficient based on peridotite xenoliths from cratons (Peslier, 2010), leading to water partition values of 1:2.7:4.7:0.2 (Ol:Opx:Cpx:Grt). The SCLM composition we considered is based on Griffin et al. (2009), where the proportions of each mineral phase have been estimated using garnet xenocrysts and xenolith suites from various representative samples of the SCLM worldwide. For discussion we consider the composition of an Archean mantle ("Primitive Archon" as in Griffin et al. (2009)): Olivine 87.8%/Orthopyroxene 10.7%/Clinopyroxene 0.3%/Garnet 1.2%/Mg# 93.1, and the composition of a Proterozoic mantle ("Preferred proton" as in Griffin et al. (2009)): Olivine 67.9%/Orthopyroxene 20.3%/Clinopyroxene 5%/Garnet 6.8%/Mg# 90.6. As seen on Fig. 8b, the difference in conductivity between Archon and Proton compositions is not strong, as we know that conductivity is weakly dependent on mineralogy (Jones et al., 2013). Therefore, from now on we will only consider the Proton composition due to the tectonic history of the region. Furthermore, since the upper and lower bounds of the associated mantle conductivity are so close, we will also only use the lower bound σ^{-}_{HS}.

As discussed in the previous section, due to the non-uniqueness of the inversion process we consider four models for the SCLM: reference model, model B, model C and model D (Figs. 5 and 7). Since those models exhibit a similar fit to the data, we decided to investigate the thermal structure and water content of the SCLM beneath the profile for all four models (Fig. 9). As mentioned above, based on the lateral changes in the resistivity beneath the profile, two different zones are considered: the Baoulé-Mossi Domain and East Baoulé-Mossi/Volta Basin (Fig. 6). The zone defined as the Baoulé-Mossi Domain includes stations bur011 to gha004 and the zone labelled East Baoulé-Mossi/Volta Basin includes stations gha005 to gha031 (Fig. 3b). Each zone is separated by the Jirapa shear zone, which appears as a significant SCLM discontinuity revealed by the 3D modelling (Figs. 5 and 6). Beneath each station of each zone, a 1D vertical resistivity profile was extracted in order to build an average resistivity profile and associated standard deviation characteristic of each area. It is worth noting that although the standard deviation is smaller in the deeper part of the profiles, it does not imply a better constraint on deeper resistivity values. It only reflects the fact the model does not vary as much at greater depth due to diminishing sensitivity combined with the inversion regularization.

There is not one model for the area but there are consistencies in our approach than can be used to draw some conclusions. Different definitions for the lithosphere asthenosphere boundary (LAB) are discussed in detail by Eaton et al. (2009). Here we are interested in resolving the electrical lithosphere-asthenosphere boundary, or eLAB. Most models agree that the lithosphere is likely cooler than the Koidu paleo-geotherm and has a thick root below the Baoulé-Mossi Domain down to at least 250 km. However, as seen for example with model C, a model associated with a shallower eLAB cannot be fully excluded. In the 3D mesh, the vertical cell dimension is about 25 km at 200–300 km depths, therefore any eLAB estimation reflect only a precision of ± 25 km. In addition, all models consistently highlight that the presence of water, well within the mantle water storage capacity at depths above 50 km (Demouchy and Bolfan-Casanova, 2016), is needed in the lithosphere to model the observed mantle resistivities. Model D of Fig. 7 shows that a model similar to the Kaapvaal with a dehydrated layer at the base of the lithosphere (Fullea et al., 2011; Peslier et al., 2010) cannot be excluded here. Whereas it is more difficult to draw conclusions about the water content, all models agree that the East Baoulé-Mossi/Volta Basin reveals a thinner and more enriched lithosphere. However, as seen on model D a thick lithosphere cannot be excluded, but the SCLM remains enriched in more conductive materials that temperature and water alone cannot

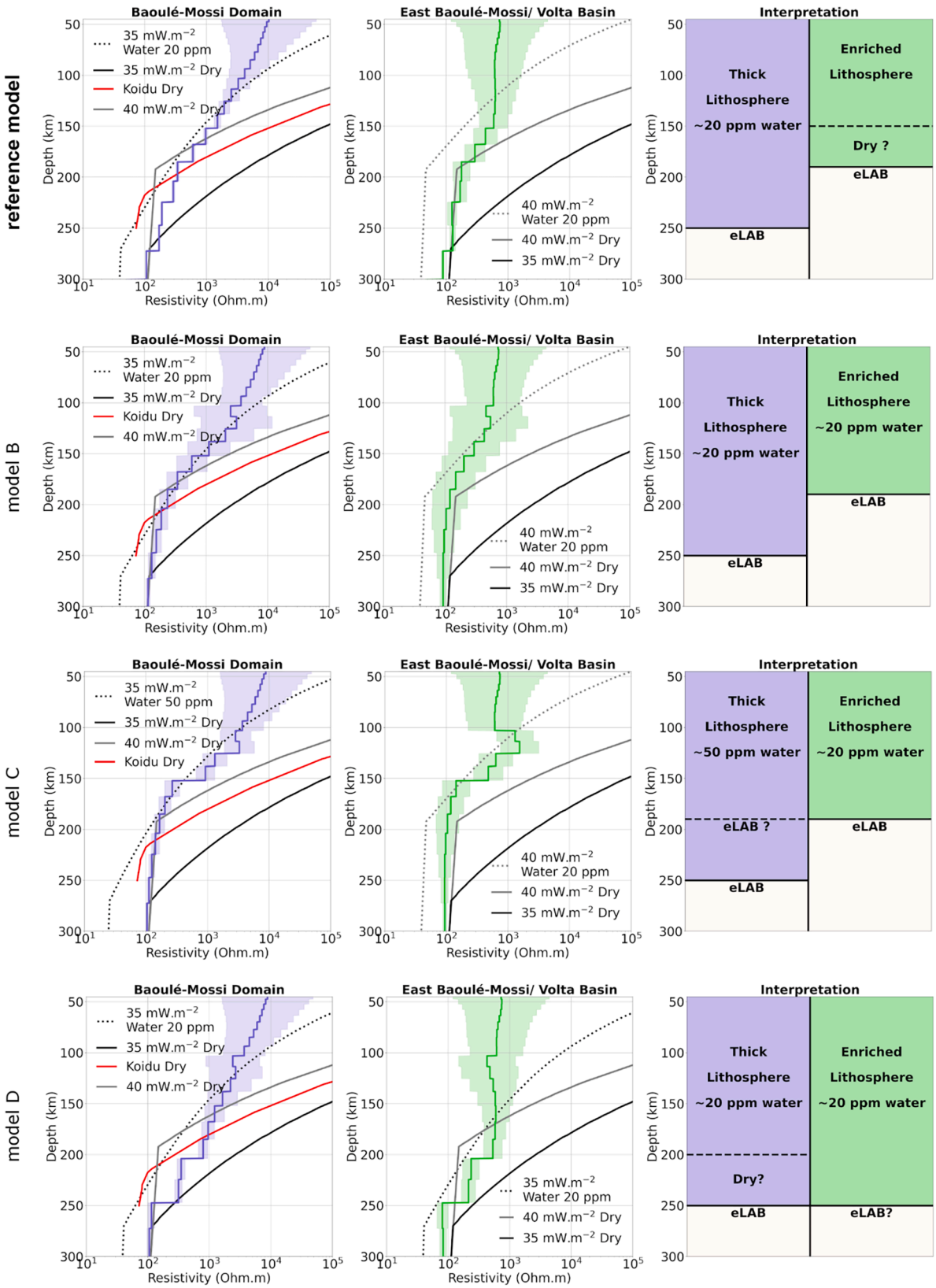

Fig. 9. Interpretation of the thermal structure and water content of the SCLM. The zone defined as the Baoulé-Mossi Domain includes stations bur011 to gha004 and the zone labelled East Baoulé-Mossi/ Volta Basin includes stations gha005 to gha031 (Fig. 6). Each zone is separated by the Jirapa shear zone. The 1D representative resistivity profiles for the Baoulé-Mossi (purple) and East Baoulé-Mossi/Volta Basin (green) are derived for the reference model (Fig. 5), model B, C and D. All models agree on a lithosphere with relatively low water content beneath the Baoulé-Mossi Domain and a potentially more enriched lithosphere beneath East Baoulé-Mossi/ Volta Basin.

explain.

It has been shown that grain boundaries can host incompatible elements in the mantle (Hiraga et al., 2004). Therefore, the electrically conductive impurities on olivine grain boundaries could explain the observed higher conductivities for the mantle. The presence of graphite films on mantle grain boundaries have been previously proposed as a good candidate to explain high conductivity values in stable regions (Bologna et al., 2011; Jones et al., 2003), however recent findings questioned the interconnection stability of graphite films along olivine grain boundary in upper mantle conditions necessary to enhance conductivity (Zhang and Yoshino, 2017). In addition, Watson et al. (2010) discussed that in comparison to carbon films, a relatively low abundance of iron sulphides on some grain boundaries significantly enhance conductivity in the upper mantle by more than one order of magnitude. As a matter of fact, the presence of sulphide mineral films in the upper mantle beneath the Volta Basin would show a good connection with the conductor located in the crust of northern Ghana (Fig. 6) if interpreted as sulphide deposits.

A decrease in grain sizes has also been proposed to account for conductive anomalies in the deep lithosphere (ten Grotenhuis et al., 2004) as the faster grain boundary diffusion begins to dominate over lattice diffusion for very fine grain sizes (Demouchy, 2010). The resulting effect on proton conduction was shown by Jones (2016). However, in their experiment ten Grotenhuis et al. (2004) used samples with grain sizes below 5 μm, meaning an extended conductive region in the deep lithosphere would need to be explained by the widespread presence of highly deformed mantle rocks or shear zones at depth where coarser grain sizes (mostly > 100 μm) would be normally expected (Demouchy, 2010; Yang and Heidelbach, 2012). Although taking into account grain boundary diffusion seems to reconcile the discrepancies in laboratory studies on proton conduction in olivine, it does not necessarily explain field observations with grain sizes still expected to be relatively coarse in the deep lithosphere, except for localized mylonized veins (Jones, 2016). Alternatively, as pyroxenites can hold two to four times more water than olivine, and as they are often observed in mantle xenoliths in veins, it is possible that wet but also Fe-rich pyroxenites dykes related to widespread enrichment of the deep lithosphere from past tectonic events provide the necessary conducting pathways (Yang and Heidelbach, 2012).

5. Discussion

The Baoulé-Mossi Domain resistivity structure fits relatively well with a low temperature geotherm (~35 mWm^{-2}), in agreement with the low heat flow values suggested by Lesquer and Vasseur (1992). In addition, the region is highly resistive throughout the whole lithosphere without any major anomalies in conductivity, a feature likely assisting its stability through time. Our interpretation of the eLAB reaching at least 250 km is also in agreement with the seismic LAB from global seismic tomography studies (Celli et al., 2020; Schaeffer and Lebedev, 2013), revealing a deep lithospheric root beneath the Leo-Man shield area, similarly to the Congo craton (Khoza et al., 2013), Kaapvaal craton (Evans et al., 2011; Muller et al., 2009) and parts of the Slave Craton and Superior Craton (Jones et al., 2003). Based on the paleo-geotherm (146 Ma) of the Koidu kimberlite showing a relatively thick lithosphere (>200 km), Smit et al. (2016) concluded that the breakup of Pangea and associated ~200 Ma Central Atlantic Magmatic Province (CAMP) (Marzoli et al., 1999) did not lead to significant lithospheric thinning or diamond destruction in the Man shield lithosphere. In addition, assuming the Koidu paleo-geotherm is representative of the south WAC at the time, the present day SCLM beneath the Leo-Man shield is likely cooler and thicker, revealing that no major events affected this part of the craton since at least the eruptions of the Jurassic kimberlites. For instance, extensive thermal perturbation from large igneous provinces (LIPs) with magma rising through the lithosphere would generate a thermal signature remaining in the lithosphere for>200 My (Jaupart and Mareschal, 2015).

It is worth noting here that the 3D inversion modelling is able to expose relative trends or lateral changes in resistivity but the high dependence on the starting/*a priori* model, as discussed by Robertson et al. (2020), leads to difficulties to make very fine interpretation on the deep mantle composition. However, we are still able to conclude that with a bulk water content of at least 20 ppm the mantle is not completely dry and even a content as high as 50 ppm cannot be totally excluded. Around the world, although the Archean Superior craton might be well described by dry olivine conductivity in the depth range of 150–250 km (Hirth et al., 2000), relatively high hydrogen content has been observed or deduced in different cratonic regions, for example in the Kaapvaal Craton (Fullea et al., 2011; Jones et al., 2012; Peslier et al., 2010). High amounts of water have been documented in the Tanzanian craton (Selway, 2015; Selway et al., 2014) and the Siberian craton (Doucet et al., 2014), suggesting that high hydrogen content does not systematically reduce plate strength but may also reflect on the role mobile belts might play in preserving the cratonic lithosphere (King, 2005; Lenardic et al., 2003). The hydrogen content in the lithosphere of the Baoulé-Mossi Domain will have been modulated through time with alternance of depletion and re-fertilization events. The Baoulé-Mossi assemblage during the Eburnean orogeny was described to have occurred in a Paleoproterozoic plate tectonics setting as a transition between Archean and Phanerozoic orogens (Baratoux et al., 2011; Block et al., 2015). This would create the hydrous environment that could explain the amount of water present in the SCLM. Furthermore, eclogitic diamond ages of ~650 Ma reported for the Leo-Man shield coincide with the Neoproterozoic assembly of Gondwana and likely originated from subduction fluids (or melts) introduced into the West African lithosphere during the supercontinent assembly (Smit et al., 2016). On the other hand, peridotitic diamonds reported from Guinea and Ghana highlight chemical depletion of the lithosphere followed by re-enrichment (Stachel et al., 2000; Stachel and Harris, 1997). In fact, since the Eburnean orogeny, eight individual dyke swarms associated with magmatic events, including the CAMP, fulfilling the size requirements for LIPs, might have affected the WAC lithosphere between 1.8 Ga and 200 Ma (Baratoux et al., 2019). The presence of a more depleted SCLM observed on the Neoproterozoic kimberlite samples compared to the Jurassic kimberlites (Skinner et al., 2004), suggests lithospheric re-enrichment might have followed the Neoproterozoic kimberlite eruption.

The East Baoulé-Mossi/Volta Basin area is likely characterised by a thinner and more enriched lithosphere, defining a transition in the lithosphere of the craton. This trend was similarly observed on the previous MT results on the WAC boundaries (Ritz and Robineau, 1988). As discussed above there are a variety of events through the craton history that can account for lithospheric thinning and re-fertilisation. However, the fact that the lithospheric transition observed on the resistivity model occurs at the proximity of the Jirapa shear zone might also imply the presence of two Eburnean domains (Jessell et al., 2016) extending into the deep mantle. This difference would follow the hypothesis of two independent cratonic blocks that might have collided during the Eburnean orogeny (Block et al., 2016). In addition, this part of the profile being relatively close to the eastern WAC boundary, lithosphere thinning and re-fertilization beneath the East Baoulé-Mossi/Volta Basin might also be explained by subduction-related metasomatism during the Pan-African orogeny. Finally, thinner lithosphere has also been recently imaged beneath the Taoudéni basin (Celli et al., 2020), highlighting a separation between the Leo-Man and Reguibat shields that could be linked to the Taoudéni sub-craton as proposed by Begg et al. (2009). This is probably extending too far in the interpretation of our model but could there be a link further in depth between the lithosphere structure of both Taoudéni and Volta Basins?

6. Conclusions

The main shear zones of the Baoulé-Mossi Domain appear as large-

scale tectonic features extending deep into the upper mantle that define the remnant signatures of the Baoulé-Mossi Domain assemblage. There is a clear lateral difference in the resistivity structure of the Baoulé-Mossi and Eastern Baoulé-Mossi/Volta Basin for both the crust and mantle that seems to be controlled by the Jirapa shear zone. To its west, the Baoulé-Mossi Domain is characterized by deep resistive roots covering the crust and most of the upper mantle. To its east, the eastern part of the domain and the Volta Basin present a more conductive crust as well as upper mantle likely revealing a change in the lithosphere composition. Although the 3D inversions performed highlight the non-uniqueness of our interpretation, due to a high dependence on the starting *a priori* model, we conclude that the lithosphere beneath the Baoulé-Mossi Domain is not dry, reflecting either the tectonic setting of the craton formation or alternance between enrichment/depletion from past tectonic events. Whereas the main domain is defined by a highly resistive, thick and cool lithosphere, its eastern edge and the Volta Basin might define a transition into a thinner and more enriched lithosphere that might have been more affected by past tectonic events.

CRediT authorship contribution statement

F. Le Pape: Visualization, Methodology, Formal analysis, Investigation, Writing - original draft. **A.G. Jones:** Supervision, Project administration, Methodology, Writing - review & editing. **M.W. Jessell:** Supervision, Funding acquisition, Project administration, Writing - review & editing. **C. Hogg:** Formal analysis, Investigation, Writing - review & editing. **L. Siebenaller:** Project administration, Writing - review & editing. **S. Perrouty:** Investigation, Writing - review & editing. **A. Touré:** Investigation. **P. Ouiya:** Investigation. **G. Boren:** Investigation.

Declaration of Competing Interest

The authors declare that they have no known competing financial interests or personal relationships that could have appeared to influence the work reported in this paper.

Acknowledgements

This work was funded by the West African Exploration Initiative (WAXI) Phase 2, and we would like to thank AMIRA International and the WAXI industry sponsors. We are also very grateful to the crews of SOS Sahel International Burkina Faso and Kalabash Ghana for their tremendous contribution in the planning and execution of the MT fieldwork but also for facilitating the communication with local villages. Special thanks to the IRD centre in Ouagadougou and particularly to Moumouni Koné and Frédéric Cazenave for their help and support during the fieldwork preparation. Thank you also to Abu Mahamud and Samuel Abanyie from the University for Development Studies, Navrongo for their involvement on the Ghanaian part of the survey. We also would like to thank Sylvain Bonvalot for helping out with the gravimeter and Saga Sawadogo from the University of Ouagadougou for the logistics on the gravity fieldwork. Thank you also to Maxim Smirnov for providing his processing code and Gary Egbert for providing the 3D inversion code ModEM3DMT. We would like to thank the Irish Centre for High Performance Computing (ICHEC) for availing the FIONN/KAY cluster to carry out the 3D inversions. Very special thanks to the local villagers for their help and welcoming during the installations of the magnetotelluric stations. Finally, we thank the editor and the two reviewers for their very helpful comments and suggestions in the revision of the manuscript.

Appendix A. Supplementary data

Supplementary data to this article can be found online at https://doi.org/10.1016/j.precamres.2021.106190.

References

Autio, U.A., Smirnov, M.Y., 2020. Magnetotelluric array in the central Finnish Lapland I: Extreme data characteristics. Tectonophysics 794, 228613. https://doi.org/10.1016/j.tecto.2020.228613.

Baratoux, L., Metelka, V., Naba, S., Jessell, M.W., Grégoire, M., Ganne, J., 2011. Juvenile Paleoproterozoic crust evolution during the Eburnean orogeny (~2.2-2.0Ga), western Burkina Faso. Precambrian Res. 191 (1-2), 18–45. https://doi.org/10.1016/j.precamres.2011.08.010.

Baratoux, L., Söderlund, U., Ernst, R.E., de Roever, E., Jessell, M.W., Kamo, S., Naba, S., Perrouty, S., Metelka, V., Yatte, D., Grenholm, M., Diallo, D.P., Ndiaye, P.M., Dioh, E., Cournède, C., Benoit, M., Baratoux, D., Youbi, N., Rousse, S., Bendaoud, A., 2019. New U–Pb Baddeleyite Ages of Mafic Dyke Swarms of the West African and Amazonian Cratons: Implication for Their Configuration in Supercontinents Through Time, in: Dyke Swarms of the World: A Modern Perspective, Springer Geology. Springer Singapore, pp. 263–314. https://doi.org/10.1007/978-981-13-1666-1_7.

Barth, M.G., Rudnick, R.L., Carlson, R.W., Horn, I., McDonough, W.F., 2002. Re-Os and U-Pb geochronological constraints on the eclogite-tonalite connection in the Archean Man Shield, West Africa. Precambrian Res. 118 (3-4), 267–283. https://doi.org/10.1016/S0301-9268(02)00111-0.

Begg, G.C., Griffin, W.L., Natapov, L.M., O'Reilly, S.Y., Grand, S.P., O'Neill, C.J., Hronsky, J.M.A., Djomani, Y.P., Swain, C.J., Deen, T., Bowden, P., 2009. The lithospheric architecture of Africa: seismic tomography, mantle petrology, and tectonic evolution. Geosphere 5, 23–50. https://doi.org/10.1130/GES00179.1.

Berryman, J.G., 1995. Mixture Theories for Rock Properties, in: Ahrens, T.J. (Ed.), Global Earth Physics: A Handbook of Physical Constants. AGU, Washington, D. C., pp. 205–228. https://doi.org/10.1029/RF003p0205.

Block, S., Ganne, J., Baratoux, L., Zeh, A., Parra-Avila, L.A., Jessell, M., Ailleres, L., Siebenaller, L., 2015. Petrological and geochronological constraints on lower crust exhumation during Paleoproterozoic (Eburnean) orogeny, NW Ghana, West African Craton. J. Metamorph. Geol. 33, 463–494. https://doi.org/10.1111/jmg.12129.

Block, S., Jessell, M., Aillères, L., Baratoux, L., Bruguier, O., Zeh, A., Bosch, D., Caby, R., Mensah, E., 2016. Lower crust exhumation during Paleoproterozoic (Eburnean) orogeny, NW Ghana, West African Craton: interplay of coeval contractional deformation and extensional gravitational collapse. Precambrian Res. 274, 82–109. https://doi.org/10.1016/j.precamres.2015.10.014.

Boher, M., Abouchami, W., Michard, A., Albarede, F., Arndt, N.T., 1992. Crustal growth in West Africa at 2.1 Ga. J. Geophys. Res. 97, 345–369. https://doi.org/10.1029/91JB01640.

Bologna, M.S., Egbert, G.D., Padilha, A.L., Pádua, M.B., Vitorello, Í., 2017. 3-D inversion of complex magnetotelluric data from an Archean-Proterozoic terrain in northeastern São Francisco Craton, Brazil. Geophys. J. Int. 210, 1545–1559. https://doi.org/10.1093/gji/ggx261.

Bologna, M.S., Padilha, A.L., Vitorello, Í., Pádua, M.B., 2011. Signatures of continental collisions and magmatic activity in central Brazil as indicated by a magnetotelluric profile across distinct tectonic provinces. Precambrian Res. 185 (1-2), 55–64. https://doi.org/10.1016/j.precamres.2010.12.003.

Bronner, G., Roussel, J., Trompette, R., Clauer, N., 1980. Genesis and Geodynamic Evolution of the Taoudeni Cratonic Basin (Upper Precambrian and Paleozoic), Western Africa. pp. 81–90. https://doi.org/10.1029/GD001p0081.

Caldwell, T.G., Bibby, H.M., Brown, C., 2004. The magnetotelluric phase tensor. Geophys. J. Int. 158, 457–469. https://doi.org/10.1111/j.1365-246X.2004.02281.x.

Carrasquilla, A., Rijo, L., 1998. Analysis of electrojet-distorted magnetotelluric sounding curves. J. Appl. Geophys. 40 (4), 187–204. https://doi.org/10.1016/S0926-9851(98)00029-9.

Celli, N.L., Lebedev, S., Schaeffer, A.J., Gaina, C., 2020. African cratonic lithosphere carved by mantle plumes. Nat. Commun. 11 (1) https://doi.org/10.1038/s41467-019-13871-2.

Curtis, S., Thiel, S., 2019. Identifying lithospheric boundaries using magnetotellurics and Nd isotope geochemistry: an example from the Gawler Craton, Australia. Precambrian Res. 320, 403–423. https://doi.org/10.1016/j.precamres.2018.11.013.

Dai, L., Karato, S., Ichiro, 2009a. Electrical conductivity of orthopyroxene: implications for the water content of the asthenosphere. Proc. Japan Acad. Ser. B Phys. Biol. Sci. 85, 466–475. https://doi.org/10.2183/pjab.85.466.

Dai, L., Karato, S., Ichiro, 2009b. Electrical conductivity of pyrope-rich garnet at high temperature and high pressure. Phys. Earth Planet. Inter. 176, 83–88. https://doi.org/10.1016/j.pepi.2009.04.002.

Demouchy, Sylvie, 2010. Diffusion of hydrogen in olivine grain boundaries and implications for the survival of water-rich zones in the Earth's mantle. Earth Planet. Sci. Lett. 295 (1-2), 305–313. https://doi.org/10.1016/j.epsl.2010.04.019.

Demouchy, S., Bolfan-Casanova, N., 2016. Distribution and transport of hydrogen in the lithospheric mantle: a review. Lithos 240–243, 402–425. https://doi.org/10.1016/j.lithos.2015.11.012.

Dentith, Michael, Yuan, Huaiyu, Johnson, Simon, Murdie, Ruth, Piña-Varas, Perla, 2018. Application of deep-penetrating geophysical methods to mineral exploration: examples from Western Australia. Geophysics 83 (3), WC29–WC41. https://doi.org/10.1190/geo2017-0482.1.

Deynoux, Max, Affaton, Pascal, Trompette, Roland, Villeneuve, Michel, 2006. Pan-African tectonic evolution and glacial events registered in Neoproterozoic to Cambrian cratonic and foreland basins of West Africa. J. African Earth Sci. 46 (5), 397–426. https://doi.org/10.1016/j.jafrearsci.2006.08.005.

Doucet, L.S., Peslier, A.H., Ionov, D.A., Brandon, A.D., Golovin, A.V., Goncharov, A.G., Ashchepkov, I.V., 2014. High water contents in the Siberian cratonic mantle linked to metasomatism: an FTIR study of Udachnaya peridotite xenoliths. Geochim. Cosmochim. Acta 137, 159–187. https://doi.org/10.1016/j.gca.2014.04.011.

Eaton, David W., Darbyshire, Fiona, Evans, Rob L., Grütter, Herman, Jones, Alan G., Yuan, Xiaohui, 2009. The elusive lithosphere-asthenosphere boundary (LAB) beneath cratons. Lithos 109 (1-2), 1–22. https://doi.org/10.1016/j.lithos.2008.05.009.

Egbert, G.D., 1990. Comments On 'Concerning dispersion relations for the magnetotelluric impedance tensor' By E. Yee and K. V. Paulson. Geophys. J. Int. 102, 1–8. https://doi.org/10.1111/j.1365-246X.1990.tb00525.x.

Egbert, G.D., Kelbert, A., 2012. Computational recipes for electromagnetic inverse problems. Geophys. J. Int. 189, 251–267. https://doi.org/10.1111/j.1365-246X.2011.05347.x.

Ennih, Nasser, Liégeois, Jean-Paul, 2008. The boundaries of the West African craton, with special reference to the basement of the Moroccan metacratonic Anti-Atlas belt. Geol. Soc. Spec. Publ. 297 (1), 1–17. https://doi.org/10.1144/SP297.1.

Evans, R.L., Jones, A.G., Garcia, X., Muller, M., Hamilton, M., Evans, S., Fourie, C.J.S., Spratt, J., Webb, S., Jelsma, H., Hutchins, D., 2011. Electrical lithosphere beneath the Kaapvaal craton, southern Africa. J. Geophys. Res. Solid Earth 116, 1–16. https://doi.org/10.1029/2010JB007883.

Ferguson, I.J., Craven, J.A., Kurtz, R.D., Boerner, D.E., Bailey, R.C., Wu, X., Orellana, M. R., Spratt, J., Wennberg, G., Norton, M., 2005. Geoelectric response of Archean lithosphere in the western Superior Province, central Canada. Phys. Earth Planet. Inter. 150 (1-3), 123–143. https://doi.org/10.1016/j.pepi.2004.08.025.

Feybesse, Jean-Louis, Billa, Mario, Guerrot, Catherine, Duguey, Emmanuel, Lescuyer, Jean-Luc, Milesi, Jean-Pierre, Bouchot, Vincent, 2006. The paleoproterozoic Ghanaian province: geodynamic model and ore controls, including regional stress modeling. Precambrian Res. 149 (3-4), 149–196. https://doi.org/10.1016/j.precamres.2006.06.003.

Fishwick, S., 2010. Surface wave tomography: Imaging of the lithosphere-asthenosphere boundary beneath central and southern Africa? Lithos 120 (1-2), 63–73. https://doi.org/10.1016/j.lithos.2010.05.011.

Fullea, J., 2017. On Joint Modelling of Electrical Conductivity and Other Geophysical and Petrological Observables to Infer the Structure of the Lithosphere and Underlying Upper Mantle, Surveys in Geophysics. Springer Netherlands. https://doi.org/10.1007/s10712-017-9432-4.

Fullea, J., Muller, M.R., Jones, A.G., 2011. Electrical conductivity of continental lithospheric mantle from integrated geophysical and petrological modeling: Application to the Kaapvaal Craton and Rehoboth Terrane, southern Africa. J. Geophys. Res. Solid Earth 116, 1–32. https://doi.org/10.1029/2011JB008544.

Fung, Agnes T., Haggerty, Stephen E., 1995. Petrography and mineral compositions of eclogites from the Koidu Kimberlite Complex, Sierra Leone. J. Geophys. Res. 100 (B10), 20451–20473. https://doi.org/10.1029/95JB01573.

Gamble, T.D., Goubau, W.M., Clarke, J., 1979. Magnetotellurics with a remote magnetic reference. Geophysics 44 (1), 53–68. https://doi.org/10.1190/1.1440923.

Garcia, X., Julià, J., Nemocón, A.M., Neukirch, M., 2019. Lithospheric thinning under the Araripe Basin (NE Brazil) from a long-period magnetotelluric survey: Constraints for tectonic inversion. Gondwana Res. 68, 174–184. https://doi.org/10.1016/j.gr.2018.11.013.

Griffin, W.L., O'Reilly, S.Y., Afonso, J.C., Begg, G.C., 2009. The composition and evolution of lithospheric mantle: a re-evaluation and its tectonic implications. J. Petrol. 50 (7), 1185–1204. https://doi.org/10.1093/petrology/egn033.

Hasterok, D., Chapman, D.S., 2011. Heat production and geotherms for the continental lithosphere. Earth Planet. Sci. Lett. 307 (1-2), 59–70. https://doi.org/10.1016/j.epsl.2011.04.034.

Heise, W., Caldwell, T.G., Bibby, H.M., Brown, C., 2006. Anisotropy and phase splits in magnetotellurics. Phys. Earth Planet. Inter. 158 (2-4), 107–121. https://doi.org/10.1016/j.pepi.2006.03.021.

Heise, W., Pous, J., 2003. Anomalous phases exceeding 90° in magnetotellurics: anisotropic model studies and a field example. Geophys. J. Int. 155, 308–318. https://doi.org/10.1046/j.1365-246X.2003.02050.x.

Hiraga, Takehiko, Anderson, Ian M., Kohlstedt, David L., 2004. Grain boundaries as reservoirs of incompatible elements in the Earth's mantle. Nature 427 (6976), 699–703. https://doi.org/10.1038/nature02259.

Hirth, Greg, Evans, Rob L., Chave, Alan D., 2000. Comparison of continental and oceanic mantle electrical conductivity: is the Archean lithosphere dry? Geochem. Geophys. Geosyst. 1 (12), n/a–n/a. https://doi.org/10.1029/2000GC000048.

Ichihara, H., Mogi, T., 2009. A realistic 3-D resistivity model explaining anomalous large magnetotelluric phases: the L-shaped conductor model. Geophys. J. Int. 179, 14–17. https://doi.org/10.1111/j.1365-246X.2009.04310.x.

Jaupart, C., Mareschal, J.C., 2015. Heat flow and thermal structure of the lithosphere. Treatise Geophys. Second Ed. 6, 217–253. https://doi.org/10.1016/B978-0-444-53802-4.00114-7.

Jessell, M., Santoul, J., Baratoux, L., Youbi, N., Ernst, R.E., Metelka, V., Miller, J., Perrouty, S., 2015. An updated map of West African mafic dykes. J. African Earth Sci. 112, 440–450. https://doi.org/10.1016/j.jafrearsci.2015.01.007.

Jessell, M.W., Begg, G.C., Miller, M.S., 2016. The geophysical signatures of the West African Craton. Precambrian Res. 274, 3–24. https://doi.org/10.1016/j.precamres.2015.08.010.

Jones, Alan G., 2016. Proton conduction and hydrogen diffusion in olivine: an attempt to reconcile laboratory and field observations and implications for the role of grain boundary diffusion in enhancing conductivity. Phys. Chem. Minerals 43 (4), 237–265. https://doi.org/10.1007/s00269-015-0790-5.

Jones, A.G., 2012. Distortion of magnetotelluric data: its identification and removal. In: Chave, A.D., Jones, A.G. (Eds.), The Magnetotelluric Method: Theory and Practice. Cambridge University Press, Cambridge (UK).

Jones, A.G., Evans, R.L., Muller, M.R., Hamilton, M.P., Miensopust, M.P., Garcia, X., Cole, P., Ngwisanyi, T., Hutchins, D., Fourie, C.J.S., Jelsma, H., Evans, S., Aravanis, T., Pettit, W., Webb, S., Wasborg, J., 2009. Area selection for diamonds using magnetotellurics: examples from southern Africa. Lithos 112, 83–92. https://doi.org/10.1016/j.lithos.2009.06.011.

Jones, Alan G., Fishwick, Stewart, Evans, Rob L., Muller, Mark R., Fullea, Javier, 2013. Velocity-conductivity relations for cratonic lithosphere and their application: example of Southern Africa. Geochem. Geophys. Geosystems 14 (4), 806–827. https://doi.org/10.1002/ggge.20075.

Jones, Alan G., Fullea, Javier, Evans, Rob L., Muller, Mark R., 2012. Water in cratonic lithosphere: Calibrating laboratory-determined models of electrical conductivity of mantle minerals using geophysical and petrological observations. Geochem. Geophys. Geosyst. 13 (6), n/a–n/a. https://doi.org/10.1029/2012GC004055.

Jones, A.G., Jödicke, H., 1984. Magnetotelluric transfer function estimation improvement by a coherence-based rejection technique, in: 54th Ann. Mtg. Soc. of Expl. Geophys. Atlanta, Georgia.

Jones, A.G., Lezaeta, P., Ferguson, I.J., Chave, A.D., Evans, R.L., Garcia, X., Spratt, J., 2003. The electrical structure of the Slave craton. Lithos 71, 505–527. https://doi.org/10.1016/j.lithos.2003.08.001.

Jones, Alan G., Spratt, Jessica, 2002. A simple method for deriving the uniform field MT responses in auroral zones. Earth, Planets Sp. 54 (5), 443–450. https://doi.org/10.1186/BF03353035.

Kalsbeek, Feiko, Frei, Dirk, Affaton, Pascal, 2008. Constraints on provenance, stratigraphic correlation and structural context of the Volta basin, Ghana, from detrital zircon geochronology: an Amazonian connection? Sediment. Geol. 212 (1-4), 86–95. https://doi.org/10.1016/j.sedgeo.2008.10.005.

Kelbert, A., Meqbel, N., Egbert, G.D., Tandon, K., 2014. ModEM: a modular system for inversion of electromagnetic geophysical data. Comput. Geosci. 66, 40–53. https://doi.org/10.1016/j.cageo.2014.01.010.

Khoza, T.D., Jones, A.G., Muller, M.R., Evans, R.L., Miensopust, M.P., Webb, S.J., 2013. Lithospheric structure of an Archean craton and adjacent mobile belt revealed from 2-D and 3-D inversion of magnetotelluric data: example from southern Congo craton in northern Namibia. J. Geophys. Res. Solid Earth 118 (8), 4378–4397. https://doi.org/10.1002/jgrb.50258.

King, S, 2005. Archean cratons and mantle dynamics. Earth Planet. Sci. Lett. 234 (1-2), 1–14. https://doi.org/10.1016/j.epsl.2005.03.007.

Kirkby, A., Zhang, F., Peacock, J., Hassan, R., Duan, J., 2019. The MTPy software package for magnetotelluric data analysis and visualisation. J. Open Source Softw. 4, 1358. https://doi.org/10.21105/joss.01358.

Krieger, L., Peacock, J.R., 2014. MTpy: a Python toolbox for magnetotellurics. Comput. Geosci. 72, 167–175. https://doi.org/10.1016/j.cageo.2014.07.013.

Le Pape, F., Jones, A.G., Jessell, M.W., Perrouty, S., Gallardo, L.A., Baratoux, L., Hogg, C., Siebenaller, L., Touré, A., Ouiya, P., Boren, G., 2017. Crustal structure of southern Burkina Faso inferred from magnetotelluric, gravity and magnetic data. Precambrian Res. 300, 261–272. https://doi.org/10.1016/j.precamres.2017.08.013.

Lenardic, A., Moresi, L.-N., Mühlhaus, H., 2003. Longevity and stability of cratonic lithosphere: Insights from numerical simulations of coupled mantle convection and continental tectonics. J. Geophys. Res. Solid Earth 108, 1–15. https://doi.org/10.1029/2002jb001859.

Lesquer, A., Beltrao, J.F., De Abreu, F.A.M., 1984. Proterozoic links between Northeastern Brazil and West Africa: a plate tectonic model based on gravity data. Tectonophysics 110 (1-2), 9–26. https://doi.org/10.1016/0040-1951(84)90055-6.

Lesquer, Alain, Vasseur, Guy, 1992. Heat-flow constraints on the West African lithosphere structure. Geophys. Res. Lett. 19 (6), 561–564. https://doi.org/10.1029/92GL00263.

Mareschal, Marianne, 1986. Modelling of natural sources of magnetospheric origin in the interpretation of regional induction studies: a review. Surv. Geophys. 8 (3), 261–300. https://doi.org/10.1007/BF01904062.

Marzoli, A., Renne, P.R., Piccirillo, E.M., Ernesto, M., Bellieni, G., De Min, A., 1999. Extensive 200-million-year-old continental flood basalts of the Central Atlantic Magmatic Province. Science (80-) 284, 616–618. https://doi.org/10.1126/science.284.5414.616.

Miensopust, M.P., Jones, A.G., Muller, M.R., Garcia, X., Evans, R.L., 2011. Lithospheric structures and Precambrian terrane boundaries in northeastern Botswana revealed through magnetotelluric profiling as part of the Southern African Magnetotelluric Experiment. J. Geophys. Res. Solid Earth 116, 1–21. https://doi.org/10.1029/2010JB007740.

Muller, M.R., Jones, A.G., Evans, R.L., Grütter, H.S., Hatton, C., Garcia, X., Hamilton, M. P., Miensopust, M.P., Cole, P., Ngwisanyi, T., Hutchins, D., Fourie, C.J., Jelsma, H.A., Evans, S.F., Aravanis, T., Pettit, W., Webb, S.J., Wasborg, J., 2009. Lithospheric structure, evolution and diamond prospectivity of the Rehoboth Terrane and western Kaapvaal Craton, southern Africa: constraints from broadband magnetotellurics. Lithos 112, 93–105. https://doi.org/10.1016/j.lithos.2009.06.023.

Naganjaneyulu, K., Santosh, M., 2012. The nature and thickness of lithosphere beneath the Archean Dharwar Craton, southern India: a magnetotelluric model. J. Asian Earth Sci. 49, 349–361. https://doi.org/10.1016/j.jseaes.2011.07.002.

Ouattara, Yacouba, Zigone, Dimitri, Maggi, Alessia, 2019. Rayleigh wave group velocity dispersion tomography of West Africa using regional earthquakes and ambient seismic noise. J. Seismol. 23 (6), 1201–1221. https://doi.org/10.1007/s10950-019-09860-z.

Padilha, Antonio L., Vitorello, Ícaro, Rijo, Luiz, 1997. Effects of the equatorial electrojet on magnetotelluric surveys: field results from Northwest Brazil. Geophys. Res. Lett. 24 (1), 89–92. https://doi.org/10.1029/96GL03792.

Pasyanos, Michael E., Nyblade, Andrew A., 2007. A top to bottom lithospheric study of Africa and Arabia. Tectonophysics 444 (1-4), 27–44. https://doi.org/10.1016/j.tecto.2007.07.008.

Patro, Prasanta K., Egbert, Gary D., 2011. Application of 3D inversion to magnetotelluric profile data from the Deccan Volcanic Province of Western India. Phys. Earth Planet. Inter. 187 (1-2), 33–46. https://doi.org/10.1016/j.pepi.2011.04.005.

Peslier, Anne H., 2010. A review of water contents of nominally anhydrous natural minerals in the mantles of Earth, Mars and the Moon. J. Volcanol. Geotherm. Res. 197 (1-4), 239–258. https://doi.org/10.1016/j.jvolgeores.2009.10.006.

Peslier, Anne H., Woodland, Alan B., Bell, David R., Lazarov, Marina, 2010. Olivine water contents in the continental lithosphere and the longevity of cratons. Nature 467 (7311), 78–81. https://doi.org/10.1038/nature09317.

Piña-Varas, P., Dentith, M., 2018. Magnetotelluric data from the Southeastern Capricorn Orogen, Western Australia: an example of widespread out-of-quadrant phase responses associated with strong 3-D resistivity contrasts. Geophys. J. Int. 212, 1022–1032. https://doi.org/10.1093/gji/ggx459.

Priestley, K., Mckenzie, D., Debayle, E., Pilidou, S., 2008. The African upper mantle and its relationship to tectonics and surface geology. Geophys. J. Int. 175, 1108–1126. https://doi.org/10.1111/j.1365-246X.2008.03951.x.

Ritz, M., Robineau, B., 1988. 1988. Tectonic Interpretation of Electrical Structures beneath the West African Craton Edge in Eastern Senegal. Am. J. Sci. 288, 756–776.

Ritz, M., 1983. The distribution of electric conductivity on the eastern border of the West African craton (Republic of Niger). Geophys. J. Int. 73 (2), 475–488. https://doi.org/10.1111/gji.1983.73.issue-210.1111/j.1365-246X.1983.tb03325.x.

Ritz, M., Robineau, B., Vassal, J., Bellion, Y., Dukhan, M., 1989. Structures of the West African Craton Margin across southern Mauritania inferred from a 450-km geoelectrical profile. Geophys. Res. Lett. 16 (4), 283–286. https://doi.org/10.1029/GL016i004p00283.

Robertson, K., Thiel, S., Meqbel, N., 2020. Quality over quantity: on workflow and model space exploration of 3D inversion of MT data. Earth, Planets Sp. 72 (1) https://doi.org/10.1186/s40623-019-1125-4.

Rooney, Alan D., Selby, David, Houzay, Jean-Pierre, Renne, Paul R., 2010. Re-Os geochronology of a Mesoproterozoic sedimentary succession, Taoudeni basin, Mauritania: Implications for basin-wide correlations and Re-Os organic-rich sediments systematics. Earth Planet. Sci. Lett. 289 (3-4), 486–496. https://doi.org/10.1016/j.epsl.2009.11.039.

Rousseeuw, Peter J., 1984. Least median of squares regression. J. Am. Stat. Assoc. 79 (388), 871–880.

Schaeffer, A.J., Lebedev, S., 2013. Global shear speed structure of the upper mantle and transition zone. Geophys. J. Int. 194 (1), 417–449. https://doi.org/10.1093/gji/ggt095.

Selway, Kate, 2015. Negligible effect of hydrogen content on plate strength in East Africa. Nat. Geosci. 8 (7), 543–546. https://doi.org/10.1038/ngeo2453.

Selway, Kate, 2014. On the causes of electrical conductivity anomalies in tectonically stable lithosphere. Surv. Geophys. 35 (1), 219–257. https://doi.org/10.1007/s10712-013-9235-1.

Selway, K., O'Donnell, J.P., Özaydin, Sinan, 2019. Upper Mantle Melt Distribution From Petrologically Constrained Magnetotellurics. Geochemistry. Geophys. Geosystems 20 (7), 3328–3346. https://doi.org/10.1029/2019GC008227.

Selway, K., Yi, J., Karato, S.I., 2014. Water content of the Tanzanian lithosphere from magnetotelluric data: Implications for cratonic growth and stability. Earth Planet. Sci. Lett. 388, 175–186. https://doi.org/10.1016/j.epsl.2013.11.024.

Siripunvaraporn, Weerachai, 2012. Three-dimensional magnetotelluric inversion: an introductory guide for developers and users. Surv. Geophys. 33 (1), 5–27. https://doi.org/10.1007/s10712-011-9122-6.

Skinner, E.M.W., Apter, D.B., Morelli, C., Smithson, N.K., 2004. Kimberlites of the Man craton, West Africa. Lithos 76 (1-4), 233–259. https://doi.org/10.1016/j.lithos.2004.04.034.

Smirnov, M.Y., 2003. Magnetotelluric data processing with a robust statistical procedure 1–7.

Smit, K.V., Shirey, S.B., Wang, W., 2016. Type Ib diamond formation and preservation in the West African lithospheric mantle: Re–Os age constraints from sulphide inclusions in Zimmi diamonds. Precambrian Res. 286, 152–166. https://doi.org/10.1016/j.precamres.2016.09.022.

Spratt, Jessica E., Skulski, Thomas, Craven, James A., Jones, Alan G., Snyder, David B., Kiyan, Duygu, 2014. Magnetotelluric investigations of the lithosphere beneath the central Rae craton, mainland Nunavut, Canada. J. Geophys. Res. Solid Earth 119 (3), 2415–2439. https://doi.org/10.1002/jgrb.v119.310.1002/2013JB010221.

Stachel, Thomas, Brey, Gerhard P., Harris, Jeff W., 2000. Kankan diamonds (Guinea) I: From the lithosphere down to the transition zone. Contrib. to Mineral. Petrol. 140 (1), 1–15. https://doi.org/10.1007/s004100000173.

Stachel, T., Harris, Jeffrey W., 1997. Syngenetic inclusions in diamond from the Birim field (Ghana) - a deep peridotitic profile with a history of depletion and re-enrichment. Contrib. to Mineral. Petrol. 127 (4), 336–352. https://doi.org/10.1007/s004100050284.

ten Grotenhuis, S.M., Drury, M.R., Peach, C.J., Spiers, C.J., 2004. Electrical properties of fine-grained olivine: Evidence for grain boundary transport. J. Geophys. Res. Solid Earth 109, 1–9. https://doi.org/10.1029/2003JB002799.

Thiel, Stephan, Goleby, Bruce R., Pawley, Mark J., Heinson, Graham, 2020. AusLAMP 3D MT imaging of an intracontinental deformation zone, Musgrave Province, Central Australia. Earth, Planets Sp. 72 (1) https://doi.org/10.1186/s40623-020-01223-0.

Thiel, Stephan, Heinson, Graham, 2013. Electrical conductors in Archean mantle-Result of plume interaction? Geophys. Res. Lett. 40 (12), 2947–2952. https://doi.org/10.1002/grl.50486.

Viljanen, A., 2012. Description of the magnetospheric/ionospheric sources. In: Chave, A. D., Jones, A.G. (Eds.), The Magnetotelluric Method: Theory and Practice. Cambridge University Press, Cambridge, U.K., pp. 96–121

Villeneuve, M., 2008. Review of the orogenic helts on the western side of the West African craton: the Bassarides, Rokelides and Mauritanides. Geol. Soc. Spec. Publ. 297, 169–201. https://doi.org/10.1144/SP297.8.

Watson, Heather C., Roberts, Jeffery J., Tyburczy, James A., 2010. Effect of conductive impurities on electrical conductivity in polycrystalline olivine. Geophys. Res. Lett. 37 (2), n/a–n/a. https://doi.org/10.1029/2009GL041566.

Wight, D., Bostick, F., 1980. Cascade decimation–A technique for real time estimation of power spectra, in: ICASSP '80. In: IEEE International Conference on Acoustics, Speech, and Signal Processing. Institute of Electrical and Electronics Engineers, pp. 626–629. https://doi.org/10.1109/ICASSP.1980.1170868.

Yamazaki, Y., Maute, A., 2017. Sq and EEJ—A Review on the Daily Variation of the Geomagnetic Field Caused by Ionospheric Dynamo Currents. Space Sci. Rev. 206 (1-4), 299–405. https://doi.org/10.1007/s11214-016-0282-z.

Yang, Xiaozhi, Heidelbach, Florian, 2012. Grain size effect on the electrical conductivity of clinopyroxene. Contrib. to Mineral. Petrol. 163 (6), 939–947. https://doi.org/10.1007/s00410-011-0707-3.

Yoshino, Takashi, Matsuzaki, Takuya, Shatskiy, Anton, Katsura, Tomoo, 2009. The effect of water on the electrical conductivity of olivine aggregates and its implications for the electrical structure of the upper mantle. Earth Planet. Sci. Lett. 288 (1-2), 291–300. https://doi.org/10.1016/j.epsl.2009.09.032.

Zhang, Baohua, Yoshino, Takashi, 2017. Effect of graphite on the electrical conductivity of the lithospheric mantle. Geochemistry. Geophys. Geosystems 18 (1), 23–40. https://doi.org/10.1002/2016GC006530.